J. Fluid Mech. (2002), *vol.* 465, *pp.* 1–32. © 2002 Cambridge University Press
DOI: 10.1017/S0022112002008935 Printed in the United Kingdom

Dynamo mechanism in a rotating spherical shell: competition between magnetic field and convection vortices

By NORIO ISHIHARA[1] AND SHIGEO KIDA[2]

[1]Department of Physics, Nagoya University, Nagoya 464-8602, Japan
[2]Theory and Computer Simulation Center, National Institute for Fusion Science,
322-6 Oroshi-cho, Toki, 509-5292, Japan

(Received 26 June 2001 and in revised form 19 February 2002)

A strong axial magnetic dipole field with magnetic energy 15 times larger than the kinetic energy of thermal convection is realized by a direct numerical simulation of the magnetohydrodynamic equation of an electrically conducting Boussinesq fluid in a rotating spherical shell which is driven by a temperature difference between the outer and inner boundaries against a gravity force pointed towards the system centre. Cyclonic and anticyclonic convection vortices are generated and play a primary role in the magnetic field intensification. The magnetic field is enhanced through the stretching of magnetic lines in four particular parts of the convection fields, namely inside anticyclones, between cyclones and their western neighbouring anticyclones at middle as well as low latitudes, and between anticyclones and the outer boundary. A 'twist-turn' loop of intense magnetic flux density is identified as a fundamental structure which yields dominant contributions both to the toroidal and poloidal components of the longitudinally averaged magnetic field. Various types of competitive interaction between the magnetic field and convection vortices are observed. Among these, a creation-and-annihilation cycle in a statistically equilibrium state is particularly important. It is composed of three sequentially recurrent dynamical processes: the generation of convection vortices by the Rayleigh–Bénard instability, the growth of anticyclones and the intensification of magnetic field by a concentrate-and-stretch mechanism, and the breakdown of vortices by the Lorentz force followed by diminution of the magnetic field. The energy transfer from the velocity to the magnetic fields takes place predominantly in this dynamical cycle.

1. Introduction

It is well known that celestial bodies have intrinsic magnetic fields. Most planets in the solar system have dipolar fields. The origin of these magnetic fields is widely believed to be the dynamo action due to convective motions of electrically conducting fluids in their interiors (see Busse 2000; Zhang & Schubert 2000; Roberts & Glatzmaier 2001 for recent reviews). Since the suggestion of this dynamo concept by Larmor (1919), the motion of an electrically conducting fluid and the generation of magnetic field by it in a rotating spherical shell have been extensively studied both theoretically and numerically. Most of the studies are based on the magnetohydrodynamic (MHD) equations of either an incompressible or compressible fluid. Regarding simulations, recent rapid developments of computer power, numerical algorithms, and visualization techniques have made it possible to increase the size of a numerical simulation and to raise the quality of data analysis. However, even now, we are still far away from the realistic direct numerical simulation of the dynamo problem because of the extremely large values of the control parameters (Merril, McElhinny & McFadden 1996; Glatzmaier & Roberts 1997).

In this situation a possible way forward is to focus our attention on the understanding of the fundamental process of the convection dynamo in a rotating spherical shell without attempting qualitative predictions, though they are of course important to perform as well. The closeness of the values of control parameters for the dynamical system and reality is then not of primary interest. Similar (but different in the type of viscosity, fluid compressibility, numerical scheme, boundary condition, etc.) convection dynamo simulations in a rotating spherical shell have been performed independently by several research groups to find common characteristics (e.g. Kageyama & Sato 1997; Kitauchi & Kida 1998; Katayama, Matsushima & Honkura 1999; Sakuraba & Kono 1999; Olson, Christensen & Glatzmaier 1999; Grote & Busse 2001). We have learned much, from these extensive simulations, on the global structure and behaviour of the convection velocity and magnetic fields in a rotating spherical shell, but not as much as on the dynamo mechanism itself. The averaged (e.g. over all longitudes) global structure of the fields is relatively easily visualized, but the instantaneous local structure, which is responsible for the dynamo action, is very hard to analyse because of the unsteadiness, irregularity and three-dimensionality of variations of the fields.

We solve here the MHD equations for an incompressible Boussinesq fluid of constant material parameters confined in a rotating spherical shell with a uniform constant temperature distribution on the boundaries under a gravity force pointing towards the system centre. This is one of the simplest non-trivial settings to study the dynamo mechanism which imitates spherical celestial bodies. Our primary interest is to find a possible mechanism for some characteristics observed in the geomagnetic field, such as the dominance of a dipole magnetic field with axis nearly parallel to the rotation axis, the intermittent irregular reversals of the dipole polarity, the spottiness of intensified magnetic regions, and so on, under the dynamo action of convective motions of an electrically conducting fluid.

In the next section a numerical model of the thermally driven MHD dynamo problem in a rotating spherical shell is introduced with fundamental equations, governing parameters, initial and boundary conditions and numerical schemes. A purely thermal convection simulation is described in § 3. Then, a dynamo simulation follows. In § 4, the dynamics of global quantities, such as the energy and the magnetic dipole moment are discussed. In § 5, the intensification mechanism of the magnetic field is presented. There are three distinct periods of temporal evolution of the magnetic field, i.e. the linear, first-equilibrium and second-equilibrium periods. After the individual dynamo mechanisms in the respective periods are described in detail, an overview of the most intensified parts of the magnetic field is given. Then, we discuss, in § 6, a competitive interaction – a creation-and-annihilation cycle of magnetic field and convection vortices. Finally, § 7 is devoted to further remarks and conclusions.

2. Spherical-shell model

We consider the magnetic field intensification by thermal convection of an electrically conducting fluid between two concentric spheres which are rotating with the same constant angular velocity $\boldsymbol{\Omega}$ around the centre. The density ρ of the fluid is assumed to be uniform and constant except in the buoyancy force term. This is the so-called Boussinesq approximation. There is a vacuum outside the outer sphere, whereas the inner sphere is filled with a perfect insulator of the same density as the fluid in the shell. The magnetic permeability μ of the vacuum, the fluid and the insulator is assumed to be the same, for simplicity. A gravity force $\boldsymbol{g}$ per unit volume acting on fluid elements is directed to the system centre and is proportional to the distance from the centre, i.e. $\boldsymbol{g} = -\gamma\boldsymbol{x}$, where γ is a constant and $\boldsymbol{x}$ is a position vector relative to the centre. Temperature is kept uniform over the two boundary spheres and constant at all times. The inner sphere is hotter than the outer by ΔT, which drives a thermal convection. Two coordinate systems, the Cartesian (x, y, z) and the spherical (r, θ, ϕ), with the origin at the centre are used where appropriate. The (x, y)-plane is taken as the equatorial plane and the z-axis as the rotation axis, whereas r is the radial, θ the co-latitudinal, and ϕ the longitudinal coordinates. In the following these coordinates systems rotate either with the spherical shell or with the convection vortices according to the circumstances.

The dynamical equations, in a frame rotating with the shell, for the fluid velocity $\boldsymbol{u}(\boldsymbol{x}, t)$, the magnetic flux density $\boldsymbol{b}(\boldsymbol{x}, t)$, and the temperature $T(\boldsymbol{x}, t)$ are given by the Navier–Stokes equation,

$$\frac{\mathrm{D}\boldsymbol{u}}{\mathrm{D}t} = -\nabla\left(\frac{p}{\rho} + \tfrac{1}{2}\gamma|\boldsymbol{x}|^2 - \tfrac{1}{2}|\boldsymbol{\Omega}\times\boldsymbol{x}|^2\right) + Pr\,Ra\,T\boldsymbol{x} + Pr\,Ta^{1/2}\boldsymbol{u}\times\hat{\boldsymbol{z}} + (\nabla\times\boldsymbol{b})\times\boldsymbol{b} + Pr\nabla^2\boldsymbol{u}, \tag{1}$$

the electromagnetic induction equation,

$$\frac{\mathrm{D}\boldsymbol{b}}{\mathrm{D}t} = (\boldsymbol{b}\cdot\nabla)\boldsymbol{u} + St\nabla^2\boldsymbol{b}, \tag{2}$$

and the heat conduction equation,

$$\frac{\mathrm{D}T}{\mathrm{D}t} = \nabla^2 T. \tag{3}$$

Since the fluid is incompressible and there is no magnetic monopole, both the velocity and magnetic fields are solenoidal,

$$\nabla\cdot\boldsymbol{u} = 0 \tag{4}$$

and

$$\nabla\cdot\boldsymbol{b} = 0. \tag{5}$$

Here, $p(\boldsymbol{x}, t)$ is the pressure, $\hat{\boldsymbol{z}} = \boldsymbol{\Omega}/|\boldsymbol{\Omega}|$ is the unit vector along the rotation axis, and $\mathrm{D}/\mathrm{D}t = \partial/\partial t + (\boldsymbol{u}\cdot\nabla)$ is the Lagrangian derivative. All the variables have been normalized in terms of the shell thickness d $(= r_2 - r_1)$, where r_1 and r_2 are the radii of the inner and outer spheres, the thermal diffusion time d^2/κ (κ being the thermal diffusivity), and the characteristic magnetic flux density $\kappa(\mu\rho)^{1/2}/d$. Four dimensionless parameters appear in these equations: the Prandtl number,

$$Pr = \frac{\nu}{\kappa}, \tag{6}$$

the Rayleigh number,

$$Ra = \frac{\alpha\gamma\Delta T d^4}{\kappa\nu}, \tag{7}$$

the Taylor number,

$$Ta = \left(\frac{2|\boldsymbol{\Omega}|d^2}{\nu} \right)^2, \tag{8}$$

and the Strebor number,†

$$St = \frac{\lambda}{\kappa}, \tag{9}$$

where α is the thermal expansion coefficient of the fluid, ν is the kinematic viscosity, and λ is the magnetic diffusivity.

These equations are solved numerically with the boundary conditions that the velocity vanishes, the magnetic field is continuous,‡ and the temperature is uniform and constant on both the inner and outer spheres. Simulations are performed by the pseudo-spectral method. All the dependent variables are expanded as spherical harmonics in the latitudinal and longitudinal directions and as Chebyshev polynomials in the radial direction. Simultaneous ordinary differential equations with respect to time for the expansion coefficients are solved by the Crank–Nicolson scheme for the diffusion terms and by the second-order Adams–Bashforth scheme for the other terms (Kitauchi, Araki & Kida 1997).

We solve the initial value problem (1)–(5) in two steps. First, (1), (3) and (4) with $\boldsymbol{b} \equiv \boldsymbol{0}$ are simulated, starting with the thermal conduction state,

$$\boldsymbol{u} = \boldsymbol{0}, \quad T = \frac{r_1}{r_2 - r_1} \left(\frac{r_2}{r} - 1 \right) \tag{10}$$

superimposed with random disturbances both in the velocity and temperature fields. The Taylor number, the Prandtl number, and the radius ratio of the two spheres are respectively set to

$$Ta = 1.6 \times 10^6, \quad Pr = 1, \quad \frac{r_1}{r_2} = 0.5. \tag{11}$$

These values are chosen as an extension of our previous studies (Kida, Araki & Kitauchi 1997; Kida & Kitauchi 1998*a*, *b*; Kitauchi & Kida 1998), namely the Taylor number is increased by factor 4 under the expectation that more intensified magnetic field may be generated. The critical Rayleigh number for the linear stability of thermal conduction state (10) at these parameters is found to be $Ra_c = 1.36 \times 10^4$. Simulations for several different supercritical Rayleigh numbers were performed. Here, we report on the case

$$Ra = 3.2 \times 10^4, \tag{12}$$

in which a strong axial magnetic dipole field is developed (Ishihara & Kida 2000). At this Rayleigh number ($Ra/Ra_c = 2.4$) the resulting thermal convection is quite irregular both in space and time.

In the second step of the simulation a random weak magnetic field is seeded in a thermal convection state obtained in the first step, and the temporal evolutions of

---

† The Roberts number Ro used in our previous papers (Ishihara & Kida 2000; Kida & Kitauchi 1998*a*, *b*; Kitauchi & Kida 1998) is renamed the Strebor number St to avoid unnecessary confusion. In Zhang & Schubert (2000), for example, the Roberts number is defined as $Ro = \kappa/\lambda$, which is the reciprocal of St. Note that the word ‘Strebor’ is the reversal of Roberts, as suggested by Professor F. H. Busse.

‡ This is the condition that there is no jump in all three components of $\boldsymbol{b}(\boldsymbol{x}, t)$, or there is no surface current, which is compatible with a finite electrical resistivity and in contrast with the vanishing Poynting flux which, as employed by Kageyama & Sato (1997), requires an unphysical infinite surface current.

the magnetic and velocity fields are traced by solving the full set of MHD equations (1)–(5). Whether the magnetic intensification is effective or not depends on the Strebor number. It is found that the magnetic field is intensified when the Strebor number is below the critical value $St_c = 0.149$. In the following we present the results for

$$St = 0.1. \tag{13}$$

The numbers of modes in the simulation are taken as $(N_r, N_\theta, N_\phi) = (129, 64, 128)$ in the radial, latitudinal and longitudinal directions, where N_r is the number of terms in the Chebyshev polynomial expansions, and N_θ and N_ϕ are the truncation orders in the spherical harmonic expansion. These numbers of modes are marginally small: halving any of them leads to either divergence of the numerical simulation or substantial truncation errors. It turns out that these truncation orders are large enough to guarantee the numerical accuracy in the sense that the peak value of the power spectra of the dependent variables drops by a factor of $10^{-2} \sim 10^{-3}$ at the cut-off mode even when the magnetic energy is highest in the present numerical simulation (cf. Christensen, Olson & Glatzmaier 1999). The time step is $\Delta t = 1.25 \times 10^{-5}$. The magnetic, viscous and thermal diffusion times are $d^2/\lambda = 10$, $d^2/\nu = 1$, and $d^2/\kappa = 1$, respectively.

The validity of our numerical code has been checked by two benchmark tests presented by Christensen *et al.* (2001). We show our results in terms of their notation. In their case 0 we obtain $E_{kin} = 58.3486$, $T = 0.43245$, $u_\phi = -10.1455$, and $\omega = 0.18240$ at resolution of $(N_r, N_\theta, N_\phi) = (33, 32, 64)$, whereas in case 1 we find $E_{kin} = 30.7741$, $E_{mag} = 626.407$, $T = 0.37336$, $u_\phi = -7.6246$, $B_\theta = -4.9288$, $\omega = -3.1018$ at $(N_r, N_\theta, N_\phi) = (33, 64, 128)$. These values agree excellently, up to three or four digits, with those listed in their tables 1 and 2, respectively. We note, in passing, that these results can be different if the initial condition is not the one specified by the benchmark test. For example, in case 0, a stationary convection velocity is not obtained if a weak random initial condition is employed, as in the present work. In case 1, the magnetic field decreases to zero if the initial magnetic field is one order of magnitude smaller than the specified value.

3. Structure of thermal convection

As described in the preceding section, the velocity field which causes the magnetic field intensification is obtained by a pure thermal convection simulation. Therefore, it is instructive to picture the characteristic properties of the structure of this thermal convection before discussion of the intensification mechanism.

An instantaneous flow structure in the fully developed thermal convection state is shown in figure 1. The grey circular annulus represents the equatorial plane, and the sphere at the centre the inner boundary of the spherical shell. The outer boundary is omitted. There are nine cyclonic and anticyclonic columns aligned alternately around the rotation axis. Besides these vortex columns the so-called Ekman boundary layers develop on the outer and inner spheres where vorticity is parallel to the boundaries and very intense. The thickness of the Ekman boundary layers on the inner and outer spheres is nearly the same and about $0.06d$, which is covered by 20 Chebyshev points in the numerical scheme, implying that these boundary layers are well resolved. The Ekman boundary layers are cut away in these figures to make the inside of the shell visible. The z-component of vorticity dominates the other components except in the Ekman boundary layers. The size and shape of iso-surfaces are different from vortex to vortex and change in time rather irregularly. Their intensity is not uniform

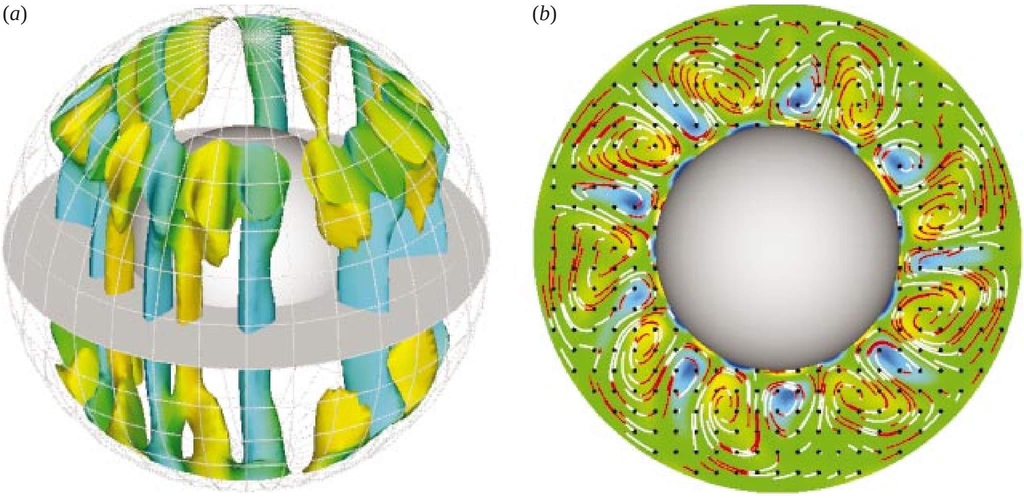

FIGURE 1. Thermal convection. (*a*) Iso-surfaces of $|\boldsymbol{\omega}|$ are drawn in yellow for cyclones ($\omega_z > 0$) and blue for anticyclones ($\omega_z < 0$). (*b*) Equatorial distribution of ω_z and streamlines. The colour map represents ω_z with yellow for positive values and blue for negative. Streamlines, which refer to the velocity field in a frame moving with the convection vortices, are drawn by coloured lines with black dots toward which the flow points. The velocity magnitude is proportional to the line length. Red and white denote respectively positive and negative accelerations along the lines.

along the axis. It is more intense near the outer boundary in cyclones, and near the equatorial plane in anticyclones. The vortices move westward with mean angular velocity $\Omega_{TP} = -3.6$ $(= -0.006\Omega)$.

The velocity field in the whole spherical shell is genuinely three-dimensional and more complicated than the vorticity field. However, the key structure, which is important for the magnetic field intensification, is relatively easily pictured by recalling the properties of the Taylor–Proudman vortex columns and the Ekman boundary layers. The cyclones (or anticyclones) are vortices of low- (or high-) pressure with swirling flows in the same (or opposite) sense as the rotation of the spherical shell and with axial flows toward (or away from) the equatorial plane, caused by the Coriolis force and the Ekman pumping.† Therefore, the flows inside both the cyclones and anticyclones are helical and skewed as a left-handed (or a right-handed) screw in the northern (or southern) hemisphere (Kitauchi *et al.* 1997). The flow pattern on the equatorial plane is simpler because the velocity field is of mirror symmetry, at least approximately. The structures of the velocity and vorticity fields on the equatorial plane are shown in figure 1(*b*). The flow is spiralling out of (or into) the cyclones (or anticyclones). This is consistent with the flows approaching (leaving) the equatorial plane in the cyclones (or anticyclones). The anticyclones are stronger and more concentrated in space than the cyclones. As will be shown in §§ 5.2 and 5.3, the magnetic field is intensified by the concentrate-and-stretch mechanism of magnetic lines in anticyclones (Kitauchi & Kida 1998).

There are two other flow patterns important for the magnetic field intensification along the outer and inner spheres, which will be discussed in § 5.1 (figure 7) and § 5.2 (figure 12).

---

† The axial flow is induced by another mechanism when the convection vortex columns are broken (§ 6.2).

4. Growth of magnetic field

The second step of the simulation described in § 2 is performed by seeding a random weak magnetic field in the thermal convection obtained in the preceding section. Initially, the Lorentz force is negligible in the Navier–Stokes equation (1) so that there is no feedback effect on the velocity field, and the induction equation (2) is linear with respect to the magnetic flux density. Since the velocity field is stationary in the statistical sense, the intensity of the magnetic field should change exponentially in time. The growth rate is a decreasing function of the Strebor number. The critical Strebor number is found to be 0.149, below which the magnetic field is intensified. In the following we report the case $St = 0.1$.

4.1. *Energy equations*

The convection dynamo is, in fact, energy transfer from the convective motion excited by the temperature difference between the inner and outer boundaries to the magnetic field. Therefore, an examination of the energy flow is useful to understand the dynamo mechanism.

The temporal evolution of the kinetic energy density per unit mass $\frac{1}{2}|\boldsymbol{u}|^2$ is derived by taking the inner product of (1) and $\boldsymbol{u}$:

$$\frac{\mathrm{D}}{\mathrm{D}t}\frac{1}{2}|\boldsymbol{u}|^2 = -\nabla\cdot\boldsymbol{u}\left(\frac{p}{\rho}+\frac{1}{2}\gamma|\boldsymbol{x}|^2-\frac{1}{2}|\boldsymbol{\Omega}\times\boldsymbol{x}|^2\right) \\ +Pr\,Ra\,T\;\boldsymbol{x}\cdot\boldsymbol{u}+\boldsymbol{u}\cdot(\boldsymbol{j}\times\boldsymbol{b})+Pr\,\boldsymbol{u}\cdot\nabla^2\boldsymbol{u}, \qquad (14)$$

where $\boldsymbol{j} = \nabla\times\boldsymbol{b}$ is the current density. The first term on the right-hand side represents the work done by the pressure, the gravity force and the centrifugal force, which integrates to zero over the spherical shell because of no-slip boundary conditions. The second term expresses the buoyancy effects which is the only source of the kinetic energy. The third term is the work done by the Lorentz force which is responsible for the direct energy exchange between the convection velocity and magnetic fields. The sign of this term turns out to be negative, which implies that kinetic energy is converted to magnetic. The last term includes all the contribution from the viscous effects, which may be written as a sum of diffusion and dissipation:

$$Pr(\nabla^2\tfrac{1}{2}|\boldsymbol{u}|^2+\nabla\nabla : \boldsymbol{uu}-2\|\mathbf{s}\|^2).$$

Here, $\mathbf{s} = \{s_{ij}\}$, $s_{ij} = \frac{1}{2}(\partial u_j/\partial x_i + \partial u_i/\partial x_j)$, $(i, j = 1, 2, 3)$ is the rate-of-strain tensor. The first two terms of this decomposition represent the diffusion, and the third the dissipation. The diffusion terms integrate to zero over the whole spherical shell. Note that the Coriolis term does not contribute to the energy dynamics at all, though it fluctuates with substantial amplitude (see (25) below).

The evolution equation for the magnetic energy density $\frac{1}{2}|\boldsymbol{b}|^2$, is derived by taking the inner product of (2) and $\boldsymbol{b}$:

$$\frac{\mathrm{D}}{\mathrm{D}t}\frac{1}{2}|\boldsymbol{b}|^2 = \boldsymbol{b}\cdot\mathbf{s}\cdot\boldsymbol{b}+St\,\boldsymbol{b}\cdot\nabla^2\boldsymbol{b}. \qquad (15)$$

The first term on the right-hand side of (15) contributes to the growth (or decay) of the magnetic energy density by stretching (or contraction) of magnetic lines. The interrelation between directions of magnetic lines and of eigenvectors with positive eigenvalues of the rate-of-strain tensor is especially important for magnetic field intensification. The second term describes the effects of diffusivity, which may be rewritten as a sum of diffusion and dissipation, e.g. $St(\nabla \cdot (\boldsymbol{b} \times \boldsymbol{j}) - |\boldsymbol{j}|^2)$. In this decomposition the first term represents the diffusion, and the second the dissipation by Joule heating. In fact, the magnetic field in the vacuum outside the spherical shell is excited through this diffusion term (see § 4.2).

4.2. *Energy dynamics*

The magnitude of variations of the velocity and magnetic fields is conveniently measured by the kinetic energy,

$$\mathscr{E}_K(t) = \tfrac{1}{2} \int_{V_{\text{shell}}} |\boldsymbol{u}|^2 \, \mathrm{d}V \tag{16}$$

and the magnetic energy,

$$\mathscr{E}_M(t) = \tfrac{1}{2} \int_{V_{\text{all}}} |\boldsymbol{b}|^2 \, \mathrm{d}V, \tag{17}$$

where V_{all} and V_{shell} denote the whole space and the spherical shell, respectively.

The evolution equation for the kinetic energy is derived by integrating (14) over the spherical shell as

$$\frac{\mathrm{d}\mathscr{E}_K}{\mathrm{d}t} = \mathscr{Q}_B - \mathscr{Q}_L - \mathscr{Q}_V, \tag{18}$$

whereas that for the magnetic energy is derived by integrating (15) over the whole space as

$$\frac{\mathrm{d}\mathscr{E}_M}{\mathrm{d}t} = \mathscr{Q}_L - \mathscr{Q}_R. \tag{19}$$

Here,

$$\mathscr{Q}_B = Pr\, Ra \int_{V_{\text{shell}}} T\, \boldsymbol{x} \cdot \boldsymbol{u} \, \mathrm{d}V \tag{20}$$

is the work done by the buoyancy force,

$$\begin{aligned} \mathscr{Q}_L &= -\int_{V_{\text{shell}}} \boldsymbol{u} \cdot (\boldsymbol{j} \times \boldsymbol{b}) \, \mathrm{d}V \\ &= \int_{V_{\text{shell}}} \boldsymbol{b} \cdot \mathbf{s} \cdot \boldsymbol{b} \, \mathrm{d}V \quad (> 0) \end{aligned} \tag{21}$$

is regarded as either minus the work done by the Lorentz force or the growth rate of the magnetic energy density by stretching of magnetic lines,

$$\mathscr{Q}_V = 2\, Pr \int_{V_{\text{shell}}} \|\mathbf{s}\|^2 \, \mathrm{d}V \tag{22}$$

is the viscous dissipation, and

$$\mathscr{Q}_R = St \int_{V_{\text{shell}}} |\boldsymbol{j}|^2 \, \mathrm{d}V \tag{23}$$

represents the resistive dissipation (the Joule heating). The positiveness of (21) is a result of the present numerical simulation. Thus, $\mathscr{Q}_L$ may represent the energy transfer rate from the velocity to the magnetic fields. Notice that the magnetic field is also being excited in the vacuum and insulator outside the spherical shell but the supply and dissipation of the magnetic energy are confined inside the shell. This implies that

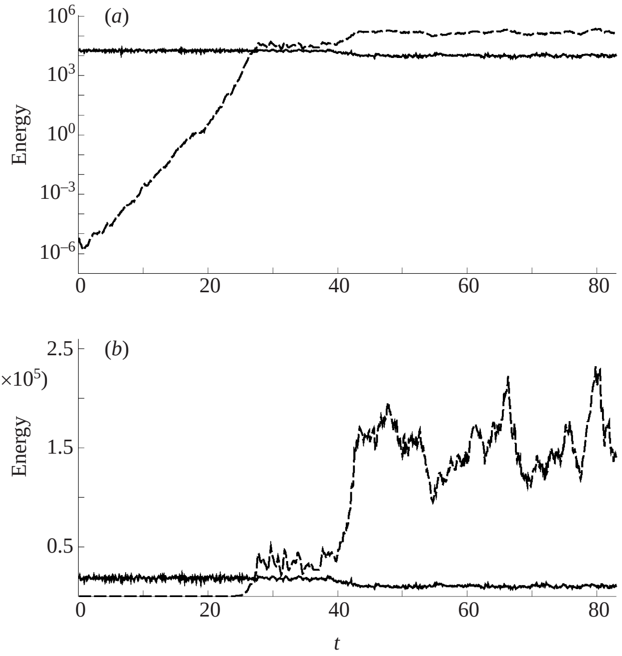

FIGURE 2. Temporal evolutions of the kinetic and magnetic energy. (*a*) Semi-logarithmic scale. (*b*) Linear scale. A solid and a broken line denote the kinetic and magnetic energy, respectively.

the flux of magnetic energy is either outward or inward through the boundaries of the spherical shell. The diffusion term, $St\nabla\cdot(\boldsymbol{b}\times\boldsymbol{j})$, in (15) is responsible for this.

Energy equations (18) and (19) provide the following scenario for the energy flux between the velocity and magnetic fields in the statistically steady state. The kinetic energy is supplied to the velocity field by the buoyancy force, part of which is dissipated by viscosity and the rest is transferred to the magnetic field through the Lorentz force. This magnetic energy is dissipated by resistivity inside the shell. The magnetic field is also excited in the vacuum and insulator outside the shell, the energy of which is typically several percent of that in the shell. The energy balance will be discussed below (see figure 3). By summing (18) and (19), we obtain the governing equation for the total energy:

$$\frac{\mathrm{d}}{\mathrm{d}t}(\mathscr{E}_K+\mathscr{E}_M)=\mathscr{Q}_B-\mathscr{Q}_V-\mathscr{Q}_R. \tag{24}$$

In figure 2, we plot the temporal evolutions of the kinetic and magnetic energy. Initially, after a short transient time ($0<t<1$), the magnetic energy increases exponentially in time with growth rate 0.78. It exceeds the kinetic energy at $t\approx 27.1$, then stops increasing at $t\approx 28$ and fluctuates around the mean value 34 800 until $t\approx 38$, which is about the double the mean kinetic energy 17 900. Those periods during which the magnetic energy increases exponentially and fluctuates around some level are called the ‘linear period’ and the ‘first-equilibrium period’, respectively. The kinetic energy is hardly different, in the mean, between the two periods, but the fluctuations are much larger in the former. A drastic change in the kinetic energy takes place at $t=41$–43, when the magnetic energy increases by factor 4.5, whereas the kinetic energy decreases by 43%. The period after this transition is called the ‘second-equilibrium period’. Figure 2(*b*) suggests quasi-periodic

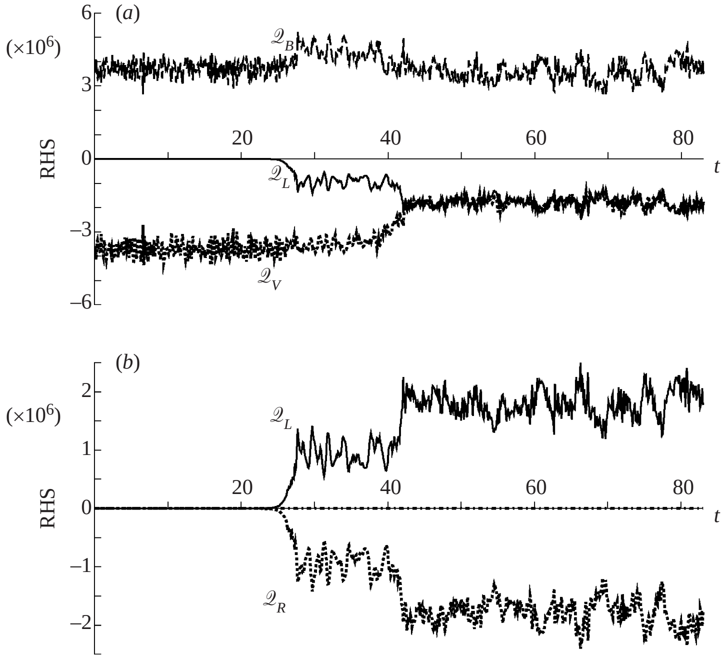

FIGURE 3. Contributions from the respective terms of the kinetic and magnetic energy equations. (*a*) Kinetic energy: $\mathcal{Q}_B$, buoyancy (– – –); $-\mathcal{Q}_L$, minus Lorentz (———); $-\mathcal{Q}_V$, minus viscous (· · · · · ·). (*b*) Magnetic energy: $\mathcal{Q}_L$, Lorentz (———); $-\mathcal{Q}_R$, minus resistive (· · · · · ·). A small fluctuating quantity seen on the abscissa denotes the sum of the energy fluxes across the outer and inner boundaries.

saw-tooth fluctuations of the magnetic energy in the second-equilibrium period. The mean magnetic energy inside the inner sphere is about 0.5%, 1% and 5% of the total in the linear, first-equilibrium and second-equilibrium periods, respectively. The corresponding values outside of the outer sphere are about 2%, 3% and 12%.

In order to see how the energy supplied by a temperature difference between the inner and outer spheres is transferred to magnetic energy, we compare, in figure 3, the time series of each term in energy equations (18) and (19). Figure 3(*a*) shows the balance in the kinetic energy equation. Throughout the simulation period the buoyancy force always gives a positive contribution which counterbalances the sum of those of the Lorentz and viscous forces. In the linear period ($t < 26$) the contributions from the buoyancy and viscous forces balance almost perfectly and the difference is less than a few percent at every instant of time. In the first- and second-equilibrium periods, on the other hand, the contribution from the Lorentz force is substantial, about 21% and 50% of that from the buoyancy force in the respective periods. The viscous dissipation is negative at all times; its magnitude hardly changes throughout the linear and first-equilibrium periods but is reduced by half in the second-equilibrium period, which is synchronized with the reduction of the kinetic energy (see figure 2). The contribution from the Lorentz force increases exponentially in time in the linear period, and its growth rate is the same as that of the magnetic field. It fluctuates around a constant level in each of the first- and second-equilibrium periods and jumps abruptly between the two periods. This abrupt change of the contribution from the Lorentz force is an indication of a difference in the dynamo mechanism

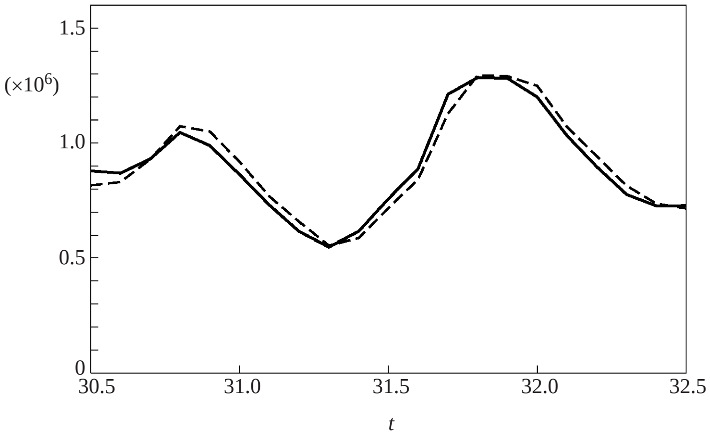

FIGURE 4. Phase lag between the stretching and resistive terms in the magnetic energy equation. Temporal variations of $\mathscr{Q}_L$ and $\mathscr{Q}_R$ are respectively plotted with a solid and a broken line for $30.5 \leqslant t \leqslant 32.5$, in the first-equilibrium period. The phase of variation of the former leads the latter by 0.03 time units.

between the first- and second-equilibrium periods (see §§ 5.2 and 5.3 below). Another noticeable jump in $\mathscr{Q}_B$ between the linear and first-equilibrium periods, which is synchronized with the variation of $\mathscr{Q}_L$, is interesting, but we have no clear-cut explanation of it.

Figure 3(*b*) for the magnetic field shows that the contribution from the stretching of magnetic lines (which is equal to that from the Lorentz force, see (21)) balances the resistive dissipation almost perfectly in the whole period. But there exists a small systematic time-lag between them. To see this, we compare, in figure 4, the temporal evolutions of $\mathscr{Q}_L$ and $\mathscr{Q}_R$ in an enlarged part of the first-equilibrium period. Their variations are very close, but the former always leads the latter by 0.03 time units. This time lag, which is much smaller than any of the magnetic, viscous and thermal diffusion times, may be interpreted as the characteristic time of the magnetic energy transfer from large-to-small scales through nonlinear interactions.

Another interesting point is that, as seen in figure 3(*a*), the contributions from the Lorentz and viscous forces are nearly equal in the second-equilibrium period. With reference to figure 3(*b*) this implies the equi-partition of energy dissipation between the velocity and magnetic fields.

Finally, a comment on the Coriolis force term may be in order. Although it does not contribute to the energy budget at all, its effects on the velocity field should be significant in the present rapid rotating system. To confirm this, we calculated the root-mean-squares (RMS) of the respective terms on the right-hand side of Navier–Stokes equation (1) over the whole of the second-equilibrium periods. The relative ratios among them are stable (fluctuations being within 5% in the standard deviation) and their time averages are found to be

$$\text{(Pressure)} : \text{(Buoyancy)} : \text{(Coriolis)} : \text{(Lorentz)} : \text{(Viscous)} = 2.0 : 1.6 : 1 : 0.7 : 0.2, \tag{25}$$

which shows that the contribution from the Coriolis term is quite large, as expected.

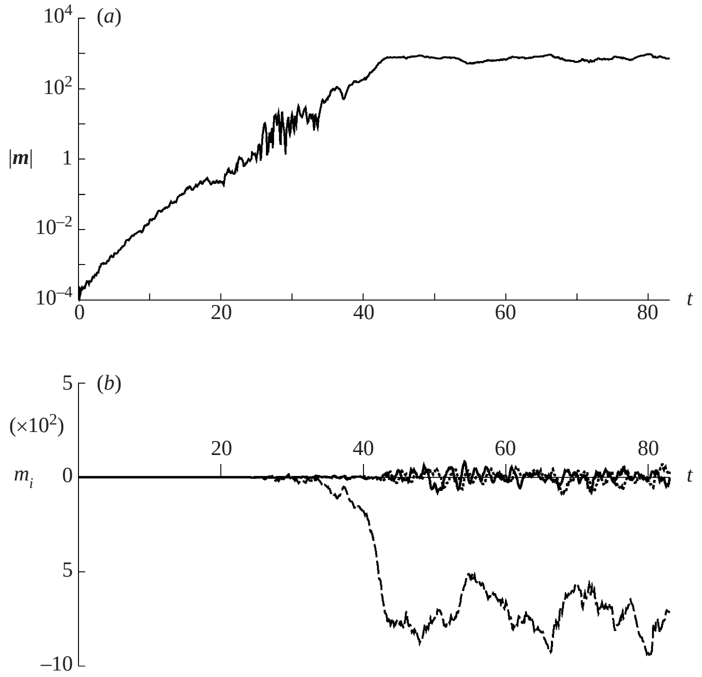

FIGURE 5. Temporal evolution of the magnetic dipole moment. (*a*) The magnitude $|\boldsymbol{m}|$ in a semi-logarithmic scale. (*b*) The x-, y-, z-components. A solid, a dotted, and a dashed line denotes m_x, m_y, and m_z, respectively.

4.3. *Magnetic dipole moment*

One of the most important quantities in magnetic field intensification is the magnetic dipole moment defined by

$$\begin{aligned}\boldsymbol{m}(t) &= \int_{V_{\text{shell}}} \tfrac{1}{2}\boldsymbol{x} \times \boldsymbol{j}(\boldsymbol{x}, t)\, \mathrm{d}V \\ &= \tfrac{3}{2}\int_{V_{\text{all}}} \boldsymbol{b}(\boldsymbol{x}, t)\, \mathrm{d}V \left(\equiv \tfrac{3}{2}\lim_{R\to\infty}\int_{V_R} \boldsymbol{b}(\boldsymbol{x}, t)\, \mathrm{d}V\right), \qquad (26)\end{aligned}$$

where V_R denotes a sphere of radius R.

The temporal evolution of the dipole moment is shown in figure 5. As seen in (*a*), the magnitude begins to increase exponentially in time and continues to grow throughout the first-equilibrium period until $t = 40$, then saturates around 800 in the second-equilibrium period. Large fluctuations of the dipole moment are observed around $t = 30$ which is the end of the linear period when the velocity and magnetic fields are about to adjust to a new state. It is seen in (*b*) that among the three components, only the z-component of the dipole moment exhibits a substantial change. It increases exponentially in time from the beginning until $t = 42$ when the system moves from the first- to the second-equilibrium periods. After $t = 30$, the z-component becomes dominant and indistinguishable from the total magnitude. The equatorial (x and y) components do not grow significantly so that the dipole moment is almost parallel to the rotation axis in the second-equilibrium period. (Although the volume integrals (26) of b_x and b_y are much smaller than that of b_z in magnitude, those of the squares of the former two are comparable with the latter. The equatorial components

Period	Linear	First-equilibrium	Second-equilibrium
Time	$1 < t < 26$	$28 < t < 38$	$t > 43$
Kinetic energy	Stationary (= 18 300)	Stationary (= 17 900)	Stationary (= 10 200)
Magnetic energy	Exponential Growth	Stationary (= 34 800)	Stationary (= 157 000)
Magnetic Reynolds number	—	350	264
Elsasser number	—	19	85
Vortex columns	Intact	Intact	Broken
Number of ACs	9	9	$4 \sim 6$
Ang. vel. of ACs	−3.5	−3.2	−2.9
Locations of intensification	(*a*), (*d*)	(*a*), (*b*), (*c*), (*d*)	(*b*), (*c*), (*d*)

Table 1. Characteristics of the magnetic field in the three periods of evolution. AC denotes anticyclones. There are four locations where the magnetic field is strongly intensified: (*a*) between a cyclone and its western neighbouring anticyclone off the equatorial plane, (*b*) inside anticyclones near the equatorial plane, (*c*) just outside the Ekman boundary layer on the outer sphere near an anticyclone, and (*d*) between a cyclone and its western neighbouring anticyclone on the equatorial plane. Here, the magnetic Reynolds number is given by $Rm = \sqrt{2\mathscr{E}_K/V_{\mathrm{shell}}}/St$ and the Elsasser number by $\Lambda = (2\mathscr{E}_M/V_{\mathrm{shell}})/(Ta^{1/2} Pr\, St)$. The ratio of the nonlinear to the resistive terms in (2) is $O(Rm)$ and that of Lorentz to the Coriolis terms in (1) is $O(\Lambda/Rm)$.

are dramatically reduced by cancellation because of their isotropic excitation.) The variation of the z-component in the second-equilibrium period is remarkably similar, apart from the sign, to that of the magnetic energy (cf. figure 2). This is consistent with the fact that strong magnetic fluxes point to the south (see § 5.3). Incidentally, the axial dipole component of the magnetic field dominates all higher-order multipoles in the second-equilibrium period, but not in the linear and first-equilibrium period.

5. Stretch and intensification of magnetic lines

We have seen in § 4 that there are three distinct periods in which the magnetic field develops in different ways. They are the linear, first-equilibrium and second-equilibrium periods. The physical characteristics in the respective periods are summarized in table 1. We consider the dynamo mechanism in each period separately in the following subsections.

5.1. *Linear period*

In an early stage of evolution the magnetic field is too weak to alter the thermal convection field through the Lorentz force. Then, the magnetic field is passively intensified by a given velocity field. Since the velocity field is not different from pure thermal convection, the characteristics of the resulting magnetic field are almost the same throughout the linear period ($1 < t < 26$): the mechanism of magnetic intensification may be understood from the pure thermal convection velocity field. The intensity of the magnetic field, such as the magnetic energy and the dipole moment, increases exponentially in time. This continues until the Lorentz force becomes strong enough to deform the velocity field.

Snapshots of the vorticity and magnetic fields in the middle of the linear period are shown in figure 6. Iso-surfaces of $|\omega_z|$ are quite similar to those in pure thermal convection (see figure 1). Regions of strong magnetic field are observed in figure 6(*a*) between cyclones and their western neighbouring anticyclones in the middle latitude

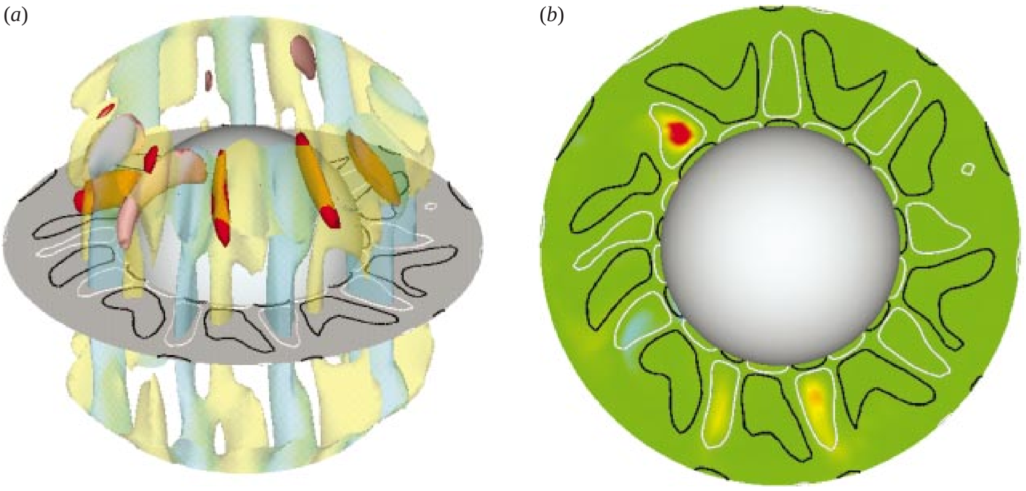

FIGURE 6. Snapshots of the vorticity and magnetic fields in the linear period. (*a*) An oblique view from 30° north latitude. The iso-surfaces of the magnetic flux density $|\boldsymbol{b}|$ are drawn with red for $b_z > 0$ and pink for $b_z < 0$, inside of which it takes larger values. Iso-surfaces of $|\omega_z|$ are drawn with yellow for cyclones ($\omega_z > 0$) and blue for anticyclones ($\omega_z < 0$). The contour level of ω_z on the equatorial plane is a somewhat lower in magnitude. The black lines are for cyclones and the white for anticyclones. (*b*) A cross-section of the fields on the equatorial plane viewed from the north. The magnetic flux density is shown with colour map in which red is for positive flux and blue is for negative. $t = 15$.

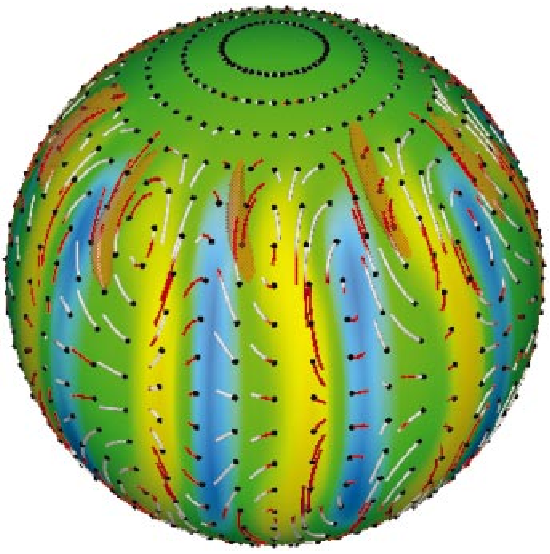

FIGURE 7. Stretching of magnetic lines between cyclones and anticyclones in the linear period. The streamlines projected on a surface of radius $r = r_1 + 0.55d$ are drawn with red-white lines and a black dot. The flow is toward the dot. The acceleration along streamlines is positive on the red part and negative on the white. The velocity field is shown in a frame moving with the convection vortices. The radial component of velocity is much smaller than the azimuthal components, as shown by colour map with blue for positive values and yellow for negative. The brown iso-surfaces represent regions of high magnetic flux density. An oblique view from 30° north latitude at $t = 15$.

(between 29° and 61°) over almost all the radial coordinate ($0.06d < r - r_1 < 0.94d$). These are the places where the flow is accelerated away from the rotation axis (see figure 7). This is consistent with the result of Kitauchi & Kida (1998) that the magnetic field is intensified where the flow points away from the rotation axis between cyclones and their western neighbouring anticyclones. In Kageyama & Sato (1997), on the contrary, the magnetic field intensification is observed at the places where the flow points toward the rotation axis. This discrepancy may be attributed to a subtle difference in the structure of the thermal convection owing to different values of control parameters.

The magnetic field is antisymmetric with respect to the equatorial plane. However, it seems a general characteristic of the present system that the magnetic field is not equally intensified between all the pairs of cyclones and their western neighbouring anticyclones but selectively between several of them (Kitauchi & Kida 1998). By comparing the iso-surfaces of the magnetic flux density at successive times (not shown here), we find that the pattern of strong magnetic regions moves westward relative to the convection vortices. In the meantime, as seen in figure 6(*b*), the magnetic field is being intensified inside anticyclones on the equatorial plane. This activity is much weaker than that in the middle latitude at this time, but it becomes more important later in the first- and second-equilibrium periods (see §§ 5.2 and 5.3).

The regions of strong magnetic field shown in figure 6 are understood by comparing them with the velocity field. In figure 7, we plot the velocity and magnetic fields at time $t = 15$ on a sphere of radius $r = r_1 + 0.55d$ where the magnetic field is strongest. The strong magnetic field is observed in accelerating regions where the magnetic lines are being stretched.

There is another intensified region, classified as (*d*) in table 1, between cyclones and their western neighbouring anticyclones on the inner-sphere side at low latitude. This region is invisible in figure 6 because it is rather narrow and the magnetic field there is a little weaker than that in (*a*). However, we have confirmed its existence at other times (cf. figure 16 in § 5.4) and identified it with the one discovered by Kitauchi & Kida (1998).

The magnetic field which has been intensified by the above mechanism deforms the velocity field through the Lorentz force and stops the growth of the magnetic field itself, and we enter the first-equilibrium period during which the magnetic energy is statistically stationary.

5.2. *First-equilibrium period*

In the first-equilibrium period ($28 < t < 38$) both the kinetic and magnetic energy are statistically stationary. The level of the mean kinetic energy is the same as that in the linear period, whereas the magnetic energy is increased to be twice as large as the kinetic. We describe in this section the structure of the velocity and magnetic fields in detail. In order to capture their temporal behaviour we show, in figure 8, a typical time sequence of the fields on the equatorial plane in this period. The time increases from (*a*) to (*f*) by 0.6 time units. These figures are plotted in a frame moving with the convection vortices which move westward with angular velocity $\Omega_{TP}(= -3.2)$ relative to the spherical shell so that each vortex is located approximately at the same position.

It is seen that all nine cyclones and anticyclones, which were present from the beginning, are robust and not destroyed though their shapes are much deformed. The individual vortices can be traced unambiguously throughout the first-equilibrium period. Note, in particular, that (i) the strong magnetic flux is confined only to the

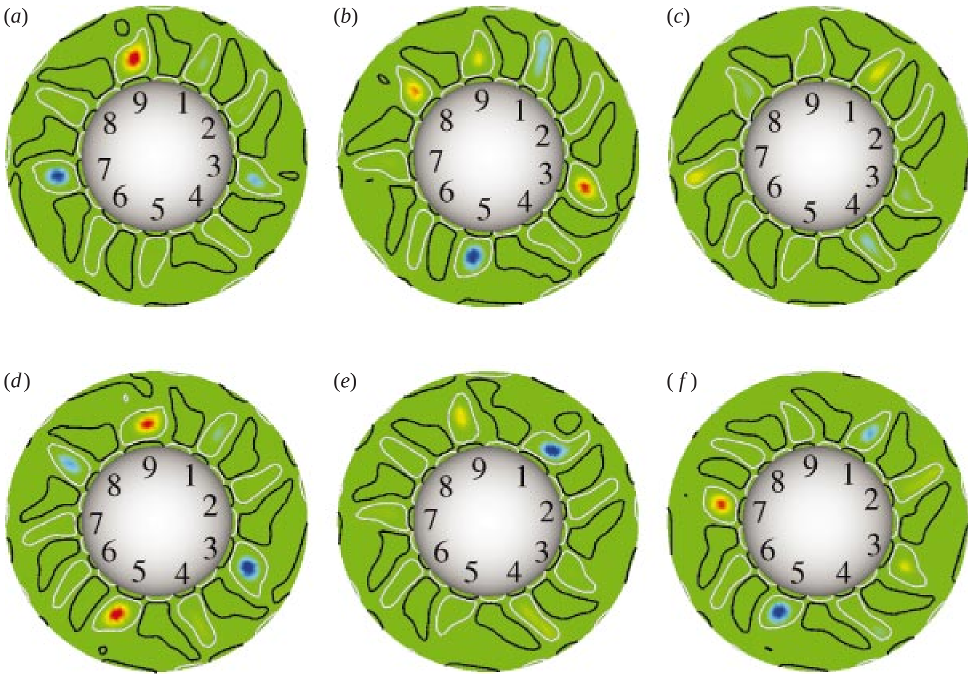

Figure 8. Temporal evolutions of the magnetic and velocity fields in the first-equilibrium period. Contour lines of ω_z are drawn with black for positive vorticity and white for negative on the equatorial plane seen from the north. The magnitude of vorticity is the same on all lines at all times. The numbers identify the individual anticyclones at different times. The colour map on the plane represents b_z, where red is for positive flux, blue is for negative, and green is for zero. (*a*) $t = 28$, (*b*) 28.6, (*c*) 29.2, (*d*) 29.8, (*e*) 30.4, (*f*) 31.

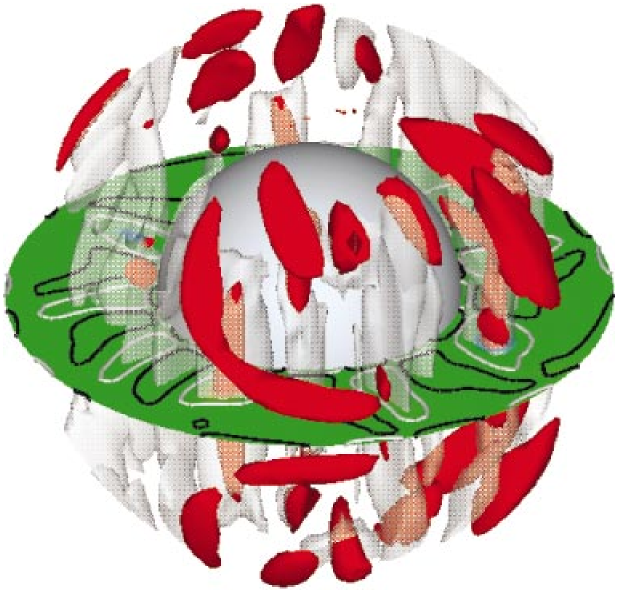

Figure 9. Snapshot of magnetic and velocity fields in the first-equilibrium period, seen from 30° north latitude. Contour lines of ω_z are drawn with black for positive vorticity and white for negative. The red surfaces represent $|\boldsymbol{b}|$ and the grey semi-transparent ones $|\boldsymbol{\omega}|$.

anticyclones, (ii) it does not occupy all anticyclones but only some of them, (iii) the intensity of the magnetic flux density in each anticyclone varies in time – some change sign before and after the magnetic flux intensity vanishes while others do not, and (iv) the shape of vorticity contours is different depending on the magnitude of magnetic field in them – the stronger the magnetic field, the rounder the shape.

Point (iii) may need an explanation. Slightly yellow anticyclone 4 in figure 8(*a*) changes to blue in (*c*), then yellow in (*e*) and blue again in (*f*). Thus, it changes sign alternately. The same behaviour is observed in five other anticyclones: 1, 3, 5, 7 and 8. The behaviour of change of sign in anticyclones 2 and 6 is similar though the intensity is rather weak. On the other hand, vortex 9 in (*a*) becomes weaker and disappears in (*c*), but reappears as the same colour in (*d*), then weakens again and disappears in (*f*).

The behaviour on the equatorial plane is simpler in appearance, but the dynamics of the system cannot be closed on this plane. The spatial distribution of iso-surfaces of $|\boldsymbol{b}|$ in the whole spherical shell is shown in figure 9 at $t = 29.8$ (corresponding to figure 8*d*), which tells us that the magnetic flux is more intense off the equatorial plane. The structure of $|\boldsymbol{b}|$ is rather complicated, but a careful inspection enables us to extract dynamically important blobs of intense magnetic field and to classify them into four groups:

(*a*) cigar-shaped ones generated at mid-latitude between a cyclone and its western neighbouring anticyclone;

(*b*) cigar-shaped ones penetrating the equatorial plane orthogonally at the centre of anticyclones;

(*c*) banana-shaped ones associated with (*b*) which are located between anticyclones and the outer boundary;

(*d*) horn-shaped ones generated at low latitude on the inner-sphere side between a cyclone and its western neighbouring anticyclone.

The first type (*a*) already exists in the linear period. The appearance of the fourth type (*d*) is very rare (cf. light-blue dots in figure 16 of § 5.4).

One of the most interesting observations discovered in a series of views (including figure 9 and others not shown here) is that the types (*b*) and (*c*) always appear together. In order to see the manner of their appearance we trace the field in detail in figure 10 which is an enlargement of a period around figure 9. First, consider the yellow anticyclone (the one numbered 5 in figure 8*a*) at the bottom left in figure 10(*a*). A banana-type blob associated with it already exists in (*a*). Then, in the following panels, a vertical cigar-type blob appears, while the banana blob is developing. They weaken in (*d*). The same process occurs with a blue anticyclone (3 in figure 8*a*) at the right in figure 9, and with a yellow anticyclone (9 in figure 8*a*) at the top in figure 9.

The directions of magnetic fluxes of these blobs are perfectly correlated with each other. In order to see the connection between the two blobs directly we show, in figure 11, the magnetic lines which go through an anticyclone at $t = 29.8$. It is seen that these lines actually run along the banana-shaped blob. The symmetry of the magnetic field with respect to the equatorial plane is still well maintained.

The formation mechanism of the banana-shaped blobs of the strong magnetic field may be seen in figure 12, where the magnetic and velocity fields on a surface just outside the Ekman boundary layer are depicted. We can see that the magnetic field is intensified along the convection flow, extending with positive acceleration both toward the south-east and the north-west from the stagnation point.

It is interesting to compare the shape of the magnetic lines shown in figure 11 with the ones discussed by Olson *et al.* (1999) as the mutual generation mechanism

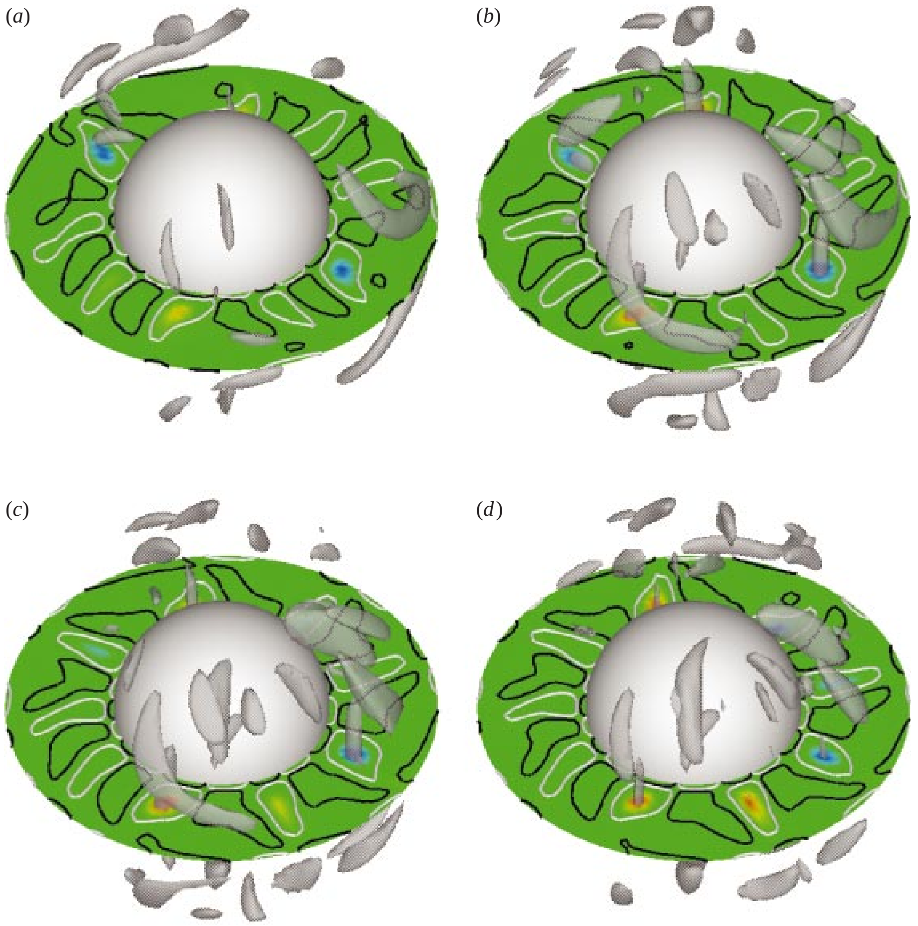

FIGURE 10. Simultaneous appearance of cigar-shaped and banana-shaped blobs of high-magnetic flux density. The grey iso-surfaces represent $|\boldsymbol{b}|$. The fields on the equatorial plane are plotted in the same manner as figure 8. (*a*) $t = 29.5$, (*b*) 29.7, (*c*) 29.9, (*d*) 30.2.

of the toroidal and poloidal fields (see figures 5 and 8 in their paper). They show a similar 'twist-turn' loop of the magnetic lines which penetrate the equatorial plane orthogonally and are twisted at a higher latitude toward the outer sphere, to the east, and to lower latitudes. Their observation of intensification by stretching of the azimuthal field component near the outer boundary corresponds to the above mechanism of generation of the banana-shaped portion.

5.3. *Second-equilibrium period*

The interaction between the velocity and magnetic fields is much more complicated in the second-equilibrium period ($t > 43$). The magnetic energy is 15 times as large as the kinetic so that the velocity field is much distorted from the pure thermal convection state. A developed magnetic field destroys the quasi-two-dimensional vortex columns along the rotation axis. On the other hand, the imposed temperature difference between the inner and outer spheres always works to generate new convection vortices. As a result, some vortices remain in the field all times. The dipole component of the magnetic flux density is dominant in this period, and the magnetic field exhibits a

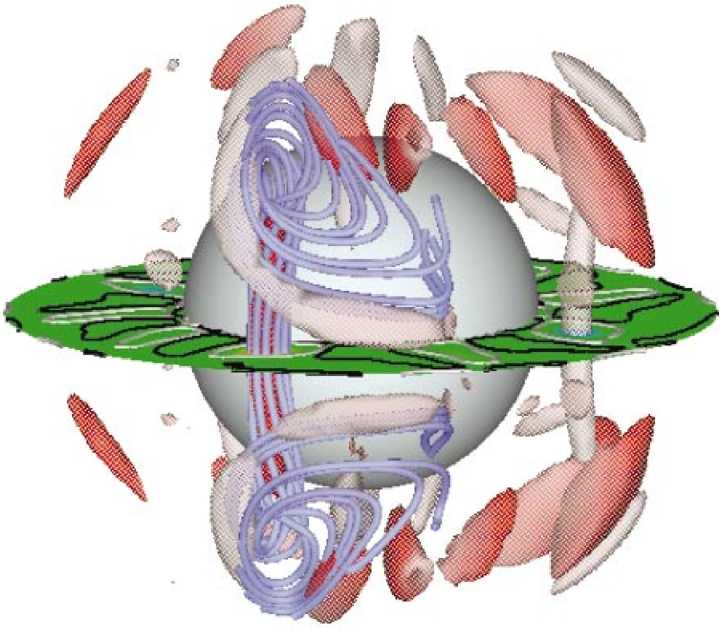

FIGURE 11. Connection between a cigar-shaped strong magnetic blob in an anticyclone and a banana-shaped one outside. Magnetic lines which go through a circle of radius $0.1d$ located at the centre of an anticyclone (5 in figure 8*d*) are drawn with blue lines. The coloured surfaces represent the iso-surfaces of $|\boldsymbol{b}|$ with red for $b_z > 0$ and pink for $b_z < 0$. $t = 29.8$.

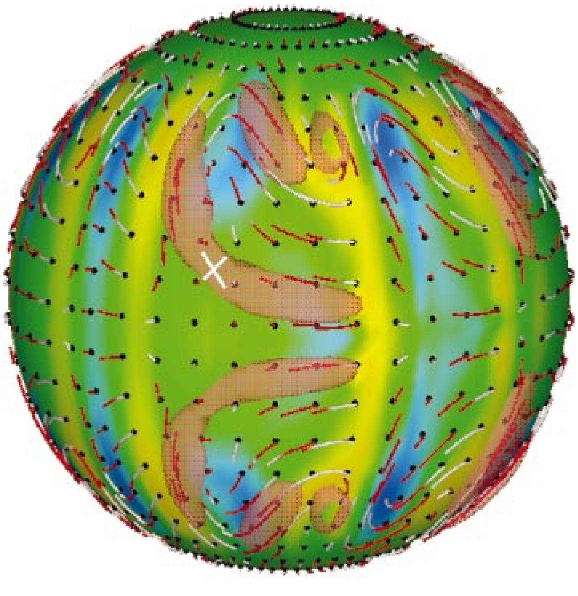

FIGURE 12. Stretch and intensification of magnetic lines near the outer sphere. Streamlines projected on a sphere of radius $r = r_1 + 0.92d$ are drawn with red-white lines and black dots, where r_1 is the inner-sphere radius and d the shell thickness. The flow, which points toward the dots, is accelerating on red lines and decelerating on white. The colour map represents the radial component of velocity with blue for positive values and yellow for negative. The magnetic flux density is stronger in the semi-transparent brown iso-surfaces. A stagnation point of the projected streamlines is indicated with white cross. $t = 29.8$.

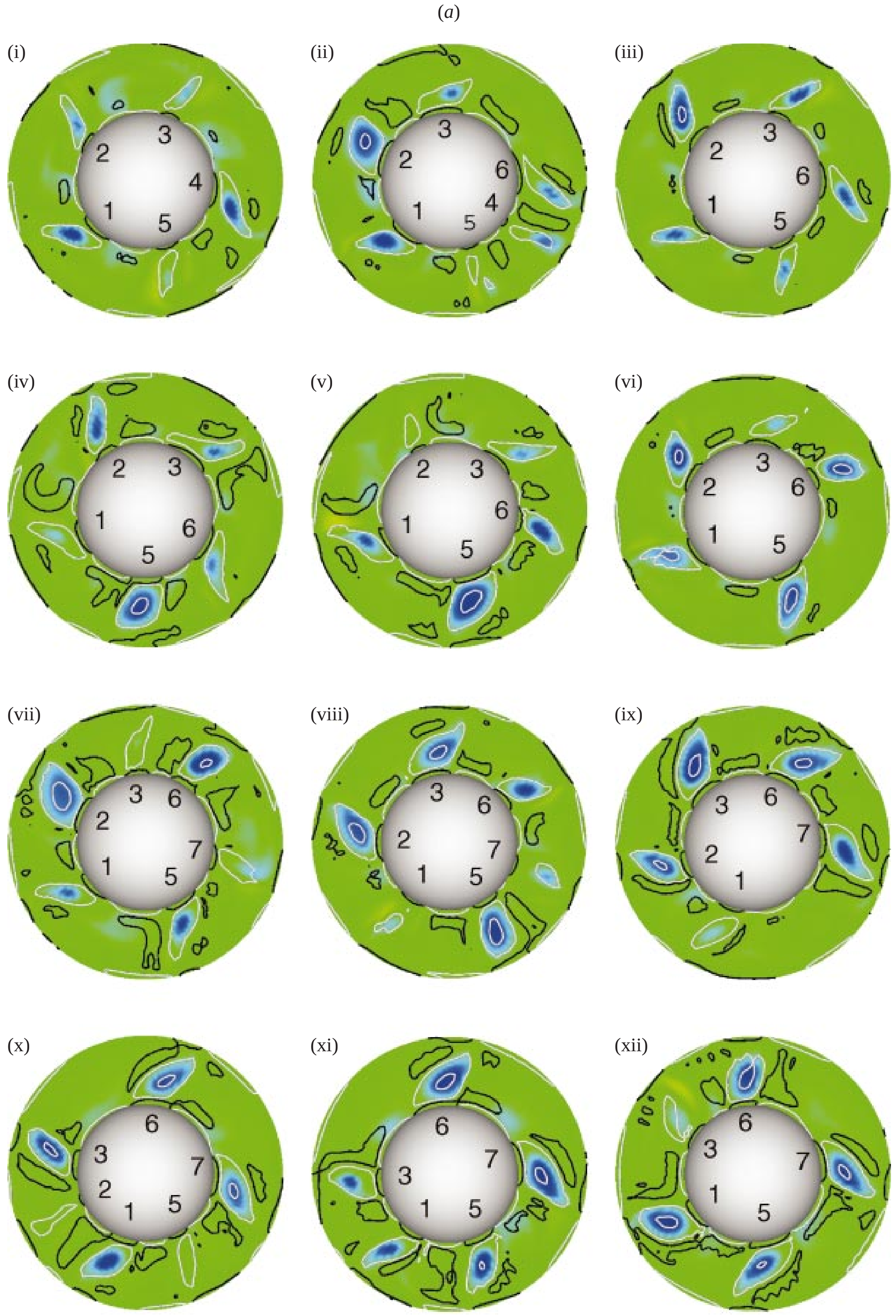

FIGURE 13(*a*). For caption see facing page.

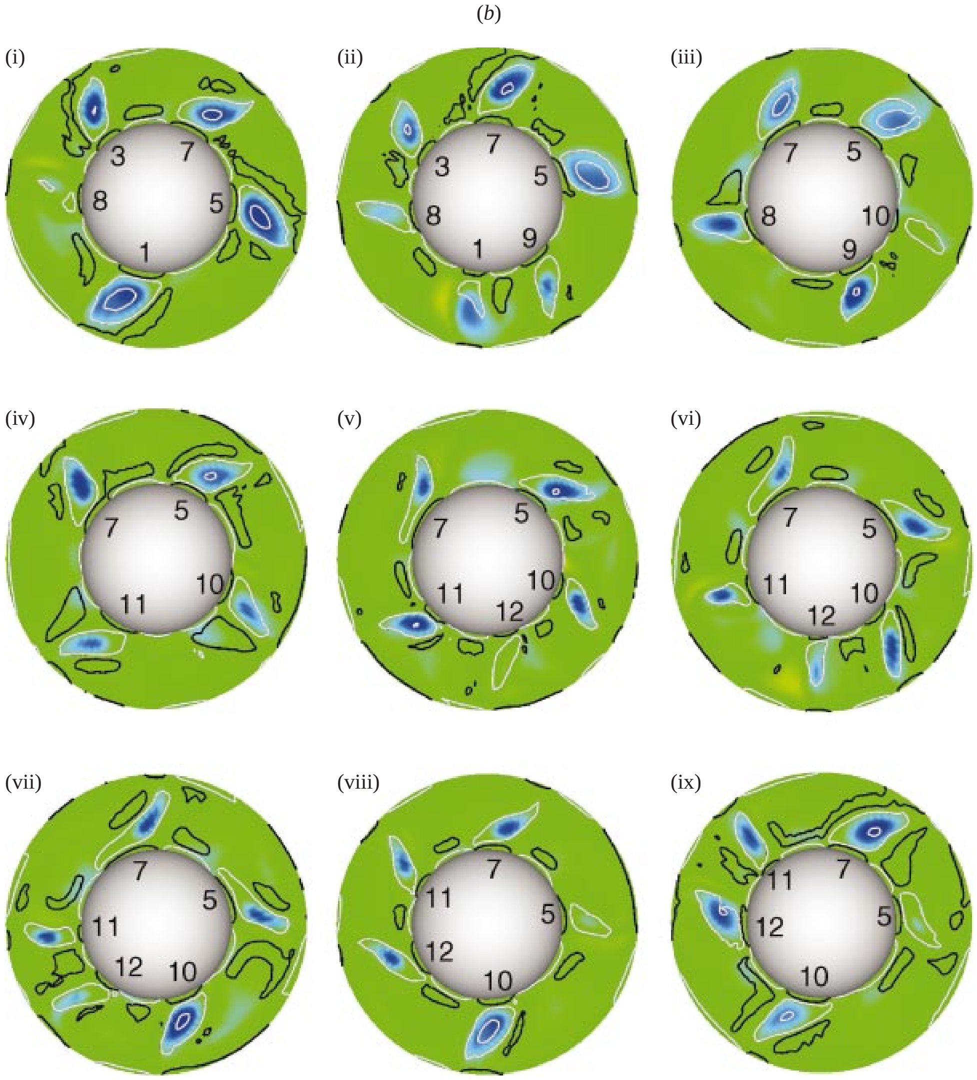

FIGURE 13. Temporal evolution of the magnetic and vorticity fields on the equatorial plane in the second-equilibrium period. (*a*) Growing-energy phase. (i) $t = 54.2$, (ii) 55.1, (iii) 56, (iv) 56.9, (v) 57.8, (vi) 58.7, (vii) 59.6, (viii) 60.5, (ix) 61.4, (x) 62.3, (xi) 63.2, (xii) 64.1. (*b*) Decaying-energy phase. (i) $t = 65.9$, (ii) 66.5, (iii) 67.1, (iv) 67.7, (v) 68.3, (vi) 68.9, (vii) 69.5, (viii) 70.1, (ix) 70.7. The representation is the same as in figure 8.

typical dipole structure in the vacuum outside the spherical shell (see figure 2 in Ishihara & Kida 2000). The axis of the dipole field is aligned with the rotation axis, so that this is called the axial magnetic dipole field.

As seen in figure 2, the magnetic energy fluctuates in time with quite large amplitude in the second-equilibrium period. The sawtooth-like oscillation observed has a period of about $15d^2/\nu$ which is comparable with the magnetic diffusion time d^2/λ $(= 10d^2/\nu)$. In order to see typical temporal evolutions of the velocity and magnetic fields we select a single time period between the first and second large minima $(54.7 < t < 66.3)$. Figures 13(*a*) and 13(*b*) show their evolutions on the equatorial plane in the growth phase ($t = 54.2$–64.1) and the decay phase ($t = 65.9$–70.7), respectively. Only a single

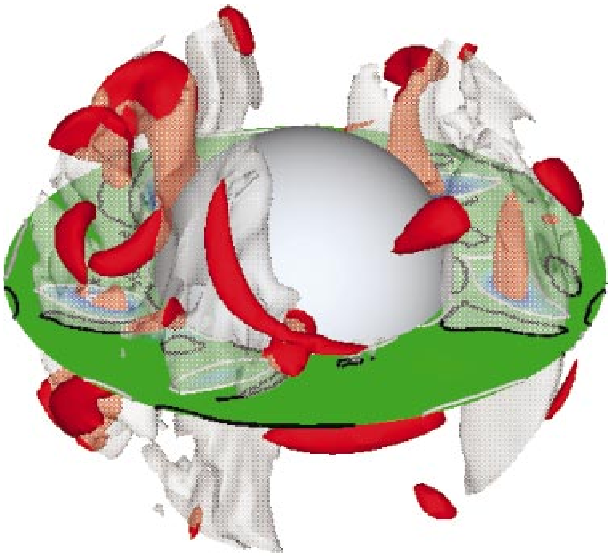

FIGURE 14. A snapshot of the magnetic and vorticity fields in the second-equilibrium period. Oblique views from 30° north latitude. The red iso-surfaces represent $|\boldsymbol{b}|$ and the grey semi-transparent ones $|\boldsymbol{\omega}|$. $t = 61.4$. The fields on the equatorial plane are the same as figure 13(*a*-ix).

level of $|\omega_z|$ is plotted on the equatorial plane so that a double contour of an anticyclone indicates the existence of a hollow at the centre. Note that the magnetic flux density b_z is negative in all the anticyclones. A snapshot of the magnetic and vorticity fields is drawn in figure 14, which corresponds to figure 13(*a*-ix).

Several interesting characteristic features are observed in these figures. First, let us focus on the vorticity field in figure 13. (i) The white contours are much wider than the black, meaning that anticyclones are much stronger than cyclones. This is a contrast to the linear and first-equilibrium periods in which the two kinds of vortices have more or less the same strength. (ii) The number of anticyclones is not invariant in time but varies between 4 and 6. They tend to arrange themselves with equi-distantly around the equatorial annulus (for example, see figure 13(*b*-iv) for the four-vortex state, figures 13(*a*-i), 13(*a*-iii) and 13(*b*-viii) for the five-vortex state, and figures 13(*a*-xii) and 13(*b*-ii) for the six-vortex state. Recall that there were nine pairs of cyclones and anticyclones in both the linear and first-equilibrium periods. This implies that a vortex breakdown should have occurred just before entering the second-equilibrium period. (iii) There are quite a few doubly-contoured anticyclones most of the time. (iv) As seen in figure 14, anticyclones are localized in the vicinity of the equatorial plane, not in the columns elongated along the rotation axis observed in the linear and first-equilibrium periods. The regions of intensified magnetic field are also different from the preceding periods. Cigar-shaped regions (classified as *b*) penetrating vertically the equatorial plane at the centres of the anticyclones are prominent. They are much stronger inside hollow vortices (see those vortices in figure 14 which correspond to 3 and 7 in figure 13). Banana-shaped regions (classified as *c*) along the outer sphere appear accompanied by the above cigars.

On the other hand, another type of cigar-shaped region (classified as *a*) between cyclones and their western-neighbouring anticyclones, which were observed in the linear and first-equilibrium periods, have disappeared. Horn-shaped regions (classified as *d*) are now seen at the eastern side of some anticyclones on the equatorial plane in figure 14.

Next, a comparison of successive snapshots of figure 13 enables us to educe some fundamental dynamical processes which are taking place in the competition between the velocity and magnetic fields. Recall that these figures are plotted in a frame rotating with the mean angular velocity -2.9 of the convection vortices so that we can identify the individual vortices. (Note, however, that now the position of vortices moves to and fro considerably because the flow motion is much more chaotic and the instantaneous angular velocity fluctuates quite a lot around the mean value.) By tracing the individual anticyclones, we find that they have a common life cycle. As stated before, the number of anticyclones changes in time between 4 and 6, which implies that they have finite lifetimes. Just after an anticyclone has disappeared, weak fluctuations of vorticity remain at the place where it was. After a while, a new anticyclone is born somewhere near that place. It develops with increasing vorticity. At the same time magnetic flux density is being intensified inside this anticyclone. Meanwhile the vorticity contours (of the same level) are doubled, meaning the appearance of a vorticity hollow at the centre. Thereafter such a double contour shows little complex behaviour. It weakens to a single contour (at the level plotted), becomes double once again, then weakens to a single, and finally disappears completely.

Let us trace some typical vortices which exhibit (a part of) the above life cycle of anticyclones. Anticyclone 6 is born in 13(*a*-ii) between 3 and 4. It is gradually intensified to grow to a hollow vortex in 13(*a*-vi). It keeps its shape for some time and then disappears between 13(*a*-xii) and 13(*b*-i). Similar behaviours are observed for other vortices except for 4 and 8. This life cycle of anticyclones will be discussed in more detail in § 6.

5.4. *Spatiotemporal overview of most intensified locations*

As seen in the preceding three subsections, there are three distinct periods in the development of the magnetic field, i.e. the linear, and first-equilibrium and second-equilibrium periods. The mechanism and location of strong magnetic field intensification are different in the respective periods. In this section we take an overview of the locations of the most intensified magnetic field over the whole volume of the spherical shell and over all the simulation period. Since the full three-dimensional structure of the magnetic field is too complicated to understand what is actually going on, it is useful to focus on and extract its most prominent characteristics. Here we discuss the spatiotemporal distributions of locations of the maximums of $|b_z|$ and $|\boldsymbol{b}|$, the former playing a key role in the interaction with the convection velocity field.

In figures 15 and 16, we plot (*a*) the latitudinal and (*b*) the radial positions of the maxima of $|b_z|$ and $|\boldsymbol{b}|$ over the whole simulation period, respectively. The maxima are sought in each hemisphere separately since the field is nearly symmetric with respect to the equatorial plane. Different colours of dots distinguish the regions of locations of the maxima.†

It is seen in figure 15(*a*) that the maxima are localized at the middle latitude ($37° \pm 6°$, where ± denotes the standard deviation) from the beginning through the end of the first-equilibrium period. The maxima are distributed symmetrically, in the statistical sense, in the northern and southern hemispheres. These are the locations (*a*) of

---

† There are a few exceptional points which are categorized wrongly by this formal criterion. For example, the lowest red point at the initial time is located just below 20° latitude (see figure 15*a*). Such points are classified appropriately by hand.

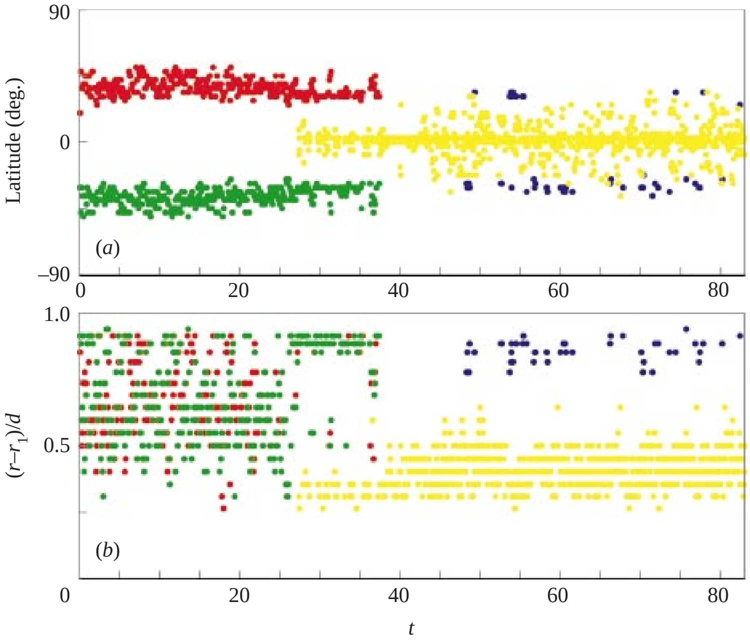

FIGURE 15. Location of the maximum of $|b_z|$, sought in each hemisphere separately. The location of the maximum is plotted with dots on (*a*) the latitudinal and (*b*) radial coordinates versus time plane. Colours distinguish the areas of locations of the maxima: red and green refer to higher latitude than 20° in the northern and southern hemispheres, respectively, at earlier times ($t < 40$), and dark blue and yellow to the outer-sphere side ($r - r_1 > 0.7d$) and the middle radial region ($0.3d < r - r_1 < 0.7d$), respectively, in the whole time period except for the red and green areas.

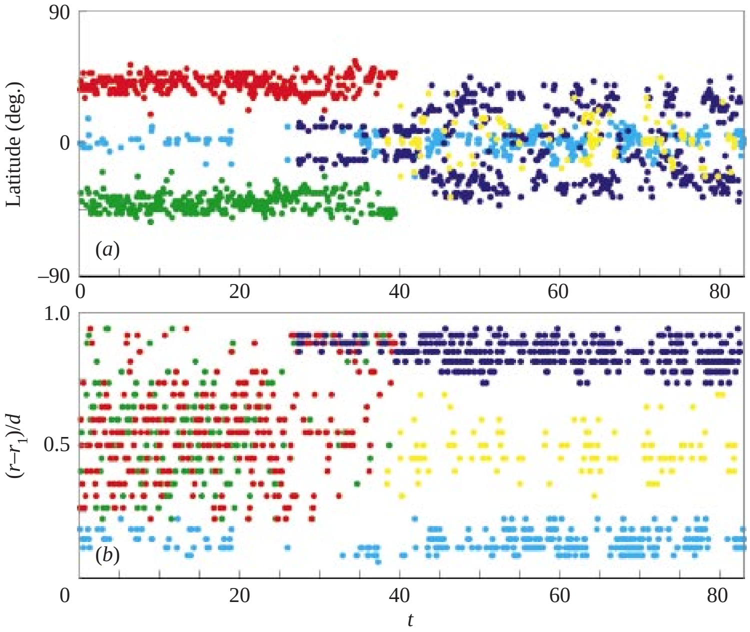

FIGURE 16. Same as figure 15 but for $|\boldsymbol{b}|$. The turquoise dots refer to the inner-sphere side (not seen in figure 15) at $r - r_1 < 0.3d$.

strong magnetic field intensification between cyclones and their western neighbouring anticyclones (see table 1 and figure 6). Their radial position is scattered over the outer half ($0.26d < r - r_1 < 0.94d$) of the spherical shell (figure 15*b*). Around $t = 28$, the beginning of the first-equilibrium period, new maxima, shown with yellow dots, appear around the middle radial region on the equatorial plane. They are localized in a narrow annulus at $0.26d < r - r_1 < 0.40d$ throughout the first-equilibrium period ($28 < t < 38$). This is the central region of anticyclones in which the magnetic field is intensified through stretching of magnetic lines perpendicularly to the equatorial plane, which is classified as (*b*) in table 1. The maxima of the part (*a*) are still observed at the same place. Coexistence of (*a*) and (*b*) is a characteristic of the first-equilibrium period (see below for the third one, *c*).

Later, in the second-equilibrium period ($t > 43$) these positions of maximum (*b*) spread out more in both the latitudinal and radial directions, which is a manifestation of more violent activity of the magnetic field. The red and green dots (maxima classified as *a*) disappear in this period. Instead, another group of maxima (shown by dark blue) appear near the outer boundary ($r - r_1 > 0.78d$) and at low latitude ($30^\circ \pm 3^\circ$), which corresponds to the banana-shaped blobs (classified as *c* in table 1) of strong magnetic field intensified along accelerating streamlines through the stagnation point just outside the Ekman boundary layer along the outer sphere. It is interesting to note that these dark blue dots appear mainly in the periods of lower magnetic energy ($50 < t < 60$ and $70 < t < 80$), while they are very rare when the activity of the magnetic field is higher ($40 < t < 50$ and $60 < t < 70$) (see figure 2).

Although $|b_z|$ is the strongest component of the magnetic field in the present system, the other components are not negligible but play substantial roles in the dynamics. In figure 16, we plot the location of the maxima of $|\boldsymbol{b}|$ in the same manner as figure 15. These two figures show both similarities and differences. The red and green dots (classified as *a*) in the linear and first-equilibrium periods are commonly observed at similar places in both figures. Also common are the groups of points appearing after around $t = 38.4$ which are plotted with yellow (classified as *b*) and dark blue dots (classified as *c*). Since the component not parallel to the rotation axis of the magnetic flux density in (*c*) is substantial, more dark blue dots are observed in figure 16. In contrast, turquoise dots are completely new in figure 16, and could not have been found without this plot. We classify this group as (*d*). These points are located near the inner core on the equatorial plane in which the component perpendicular to the rotation axis of the magnetic flux density is dominant. This is located between cyclones and their western neighbouring anticyclones (see the equatorial plane on the inner-sphere side in figure 14). This is the same as that observed in Kitauchi & Kida (1998) in the case of weak magnetic field, which is also generated by the concentration and stretching of magnetic lines.

6. Competition between magnetic field and convection vortices

As seen in § 5.3, there is an interesting dynamical competition between anticyclonic vortex blobs and the magnetic field which repeats cyclically in time. A single cycle is composed of three elementary processes, which are (i) the birth of convection vortices, (ii) the growth of anticyclones together with the intensification of magnetic field therein, and (iii) the breakdown of anticyclones and the diminution of magnetic field. In the following we consider the dynamical mechanism in each of these processes separately.

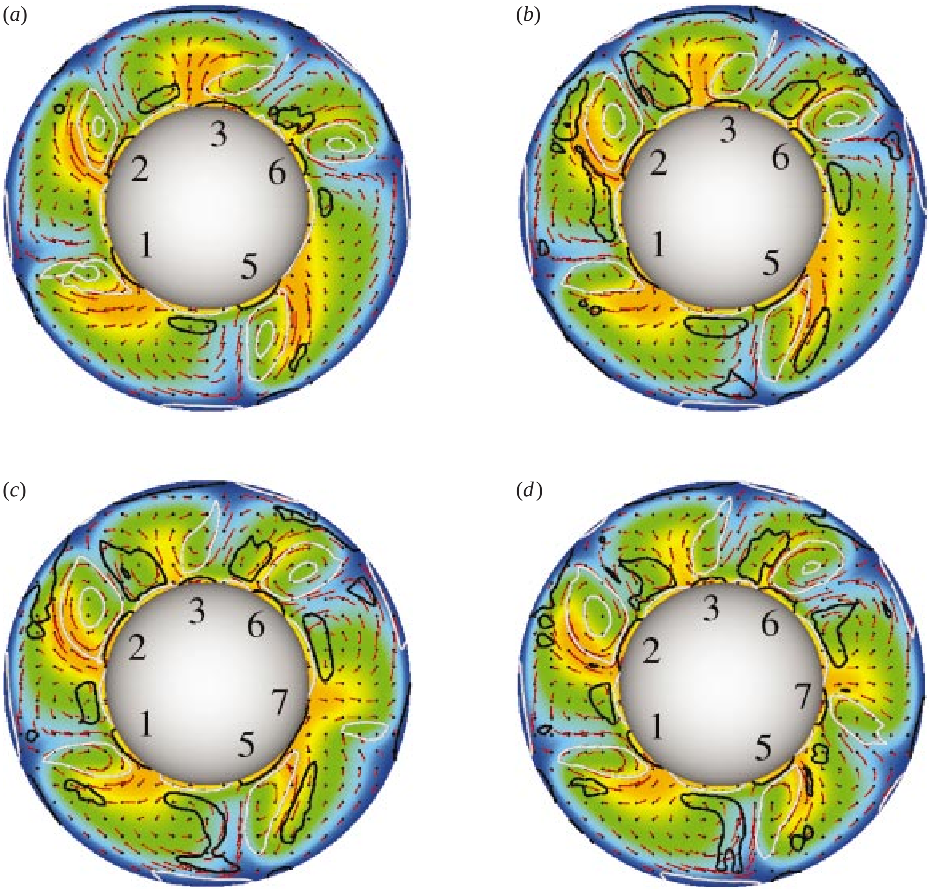

FIGURE 17. Birth of an anticyclone. Streamlines are represented on the equatorial annular plane by brown lines with black dots toward which the flow points. Vorticity contours are drawn with black for $\omega_z > 0$ and white for $\omega_z < 0$. Only a single value of the vorticity magnitude $|\omega_z|$ is chosen for the contours. Colour map shows the temperature distribution with red for hot areas and blue for cold. (*a*) $t = 58.7$, (*b*) 59.1, (*c*) 59.5, and (*d*) 59.6.

6.1. *Birth of convection vortices*

First, we recall that there is a steady driving force caused by a temperature difference between the inner and outer spheres against the gravity force pointing at the system centre. Since the cyclic process is repeated, one can begin with any step of the cycle. We start by considering the birth of an anticyclone. Figure 17 is a typical time series which shows the birth of an anticyclone. Time increases from (*a*) to (*d*), which is a subdivision of the period between figures 13(*a*-vi) and 13(*a*-vii). The temperature distribution is represented by colour map with red for hotter areas and blue for cooler. There are five strong anticyclones in (*a*), all of which wrap high-temperature fluid blobs on their east side. Cyclones of much weaker intensity accompany most of the anticyclones. The five anticyclones are more or less equally separated from each other. Notice, however, that the distance between anticyclones 5 and 6 is slightly longer than the others, and increases as time progresses from (*b*) to (*d*). In the meantime, high-temperature fluid blobs extend along the hot inner boundary, and at the same time a cyclone adjacent to anticyclone 6 grows. A new anticyclone 7 is born and grows in (c) and (d). This is in fact the Rayleigh–Bénard instability mechanism of thermal convection. Soon afterwards, this new anticyclone grows to a strong one, whereas the neighbouring cyclone weakens (see figure 13(a-ix)–(a-xii)).

This birth process of a new anticyclone is often observed. See, for example, the ones labelled 6 in figure 13(a-ii), 8 in figure 13(b-i), 9 in figure 13(b-ii), and 10 in figure 13(b-iii). The one labelled 5 in figure 13(a-x) seems to have been generated in the same way as the above but since it was born at the place where a strong anticyclone had broken down (see 5 in figure 13(a-viii)), we assign the same number, 5, to it.

6.2. *Growth of anticyclones and intensification of magnetic field*

It is observed in the second-equilibrium period that the anticyclones are much stronger in intensity than the cyclones. The primary cause is the local enhancement, near the equatorial plane, of the Coriolis force, which points towards (or away from) the centre of anticyclones (or cyclones), and therefore the pressure tends to be higher (or lower) inside anticyclones (or cyclones). Since the flow in the second-equilibrium period is rather unstable and genuinely three-dimensional (unlike the linear and first-equilibrium periods), the above dynamical process is taking place mostly near the equatorial plane. Thus, the high-pressure blobs inside anticyclones are pushed to higher latitudes (i.e. away from the equatorial plane), and vice versa inside cyclones. This mechanism of inducing the axial flow inside the convection vortices is different from that due to the Ekman pumping on the outer boundary which is applied to a quasi-two dimensional flow along the rotation axis of the spherical shell in the linear and first-equilibrium periods.†

Anticyclones draw fluid elements spirally into themselves in the equatorial plane and push them up along their rotation axes helically. Advected by this flow, both vorticity and magnetic lines are concentrated at the centre of anticyclones on the equatorial plane and stretched along their rotation axes. In figure 18, we plot streamlines around an anticyclone (which is 7 in figure 13(a-ix)) together with magnetic lines which pass through the central region of the anticyclone. It is seen that the magnetic flux is transported toward the centre along the equatorial plane, which is then stretched in the direction perpendicular to the equatorial plane. This concentration and stretching of magnetic lines is observed in every anticyclone and must be the main mechanism of the magnetic field intensification (Kitauchi & Kida 1998).

6.3. *Breakdown of anticyclones and diminution of magnetic field*

As discussed in the preceding section the magnetic field is intensified by stretching of magnetic lines inside anticyclones. But this cannot continue forever. The intensified magnetic field concentrated in a tube region induces an electric current around it by Ampère's law, which couples with the surrounding magnetic field to generate a Lorentz force in the outward radial direction. As a result, the flow into anticyclones is weakened, the vorticity magnitude at the centre is lowered to make the anticyclones hollow and eventually lead to a breakdown. Then, the magnetic field dies away because it loses the support. (On the other hand, Sakuraba & Kono (1999) were lead to a conclusion that the Lorentz force works to enhance anticyclones under the premise of the presence of lower pressure at the centre of anticyclones to counterbalance the outward Lorentz force. Note, however, that there is no reason to assume this force balance *a priori*.)

---

† The induced axial flow is also explained by the local enhancement (or suppression) of thermal torque in anticyclones (or cyclones) in the vorticity equation (Olson *et al.* 1999, p. 10390).

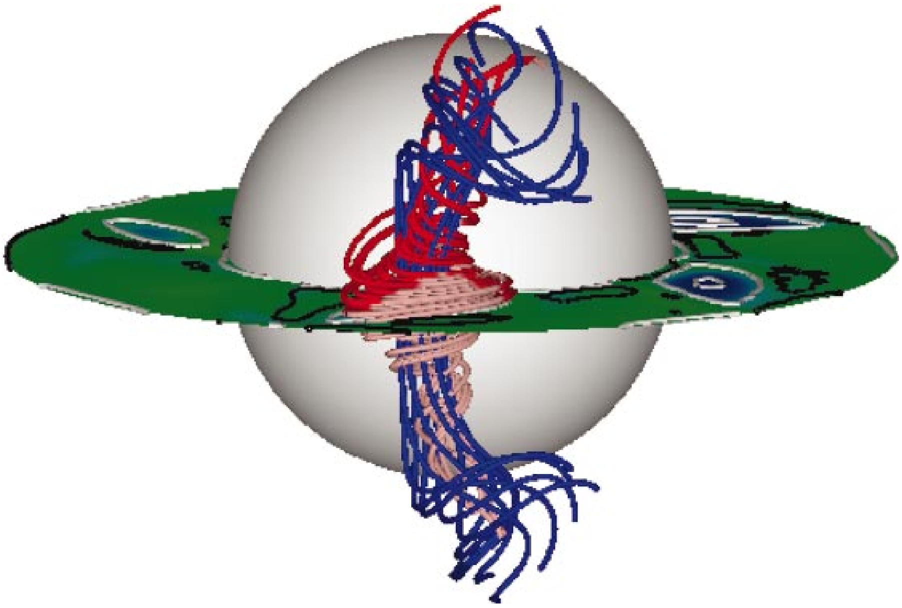

Figure 18. Intensification of magnetic field by stretching. Magnetic lines which pass through an anticyclone (7 in figure 13(a-ix) viewed from the right) are drawn with blue lines, the magnetic flux of which points to the south. Helical lines surrounding the magnetic lines represent streamlines. The red and pink indicate the northward and southward flows, respectively. Viewed from 10° north-latitude at $t = 61.4$.

Figure 19. Lorentz force on the equatorial plane. Red lines with a white dot represent the lines of Lorentz force directed towards the dot. The z-component of vorticity is shown by contours, with black for cyclones and white for anticyclones. The magnitude of all the contours is the same. Colour map represents the z-component of magnetic field with red (hardly seen) for $b_z > 0$ and blue for $b_z < 0$. Viewed from the north at $t = 62.3$.

The situation that anticyclones having strong magnetic field in them are suffering from the Lorentz force directed to the outward radial directions is shown in figure 19, which is a snapshot at $t = 62.3$. There are four double-contour anticyclones having strong southward magnetic field in them. The Lorentz force is very strong inside these anticyclones and pointed to the outward radial directions. We can also see that the Lorentz force is pointed to the inward in cyclones represented by black lines. Similar behaviours are observed on other planes $z = const.$ parallel to the equatorial plane at least where $|z| < 1$.

At the place where an anticyclone has broken down and the magnetic field has disappeared only weak random fluctuations of vorticity and magnetic flux are left. Thereafter, sooner or later, a new anticyclone is created by the Rayleigh–Bénard instability (see § 6.1), and the dynamical process will be repeated.

This stage of the birth of a new convection vortex may play a key role with relation to the magnetic field reversal. This is because the direction of the magnetic field may be determined by a random sign of a weak magnetic field. Since the remnant of the previous magnetic field has some influence on the next sign, some violent event of substantial strength may be necessary to change the sign. This scenario is not observed in the present numerical simulation, but it might occur in a longer run.

7. Concluding remarks

The convection dynamo in a rotating spherical shell has been investigated numerically and visually with the aim of finding a mechanism of magnetic field intensification. There are several different types of interactions between the convection vortices and the magnetic field at different places and times, whereas the stretching of magnetic lines is the common mechanism of magnetic field intensification. Among others, a recurrent cycle of interaction between convection vortices and magnetic field observed in the second-equilibrium period, in which the magnetic energy is 15 times larger than the kinetic energy of thermal convection, is particularly interesting and important. It consists of three elementary dynamical processes: the birth of the convection vortices through the Rayleigh–Bénard instability; the growth of anticyclones and the intensification of magnetic field therein by the concentrate-and-stretch mechanism; and the breakdown of anticyclones through the Lorentz force induced by the intensified magnetic field. The transfer of magnetic energy to kinetic takes place mostly in this recurrent cycle of creation and annihilation of convection vortices and magnetic field.

Because of complexity of the spatiotemporal behaviour of velocity and magnetic fields their longitudinal averages have often been investigated as a simplified representation of the full three-dimensional structure. However, many numerical simulation analyses not only confirm that the fields are far from axisymmetric (i.e. the Cowling theorem) but also show that the dynamo action is a local phenomenon. A correct dynamo mechanism could be identified only by looking carefully at the local instantaneous structures of the velocity and magnetic fields. For example, a banana-shaped blob of intense magnetic field always appears together with a cigar-shaped one inside an anticyclone in the above recurrent dynamical process. These two blobs are connected to make a ‘twist-turn’ loop of intense magnetic flux density. This unique loop constitutes a key structure in the sense that it makes the main contribution, after a longitudinal average, to the commonly observed dipole pattern of the poloidal components of the magnetic field and the bull’s-eyes pattern of the toroidal component.

In figure 20, we plot the longitudinal average of (*a*) the velocity and (*b*) magnetic fields at some time instant in the second-equilibrium period. The longitudinal and

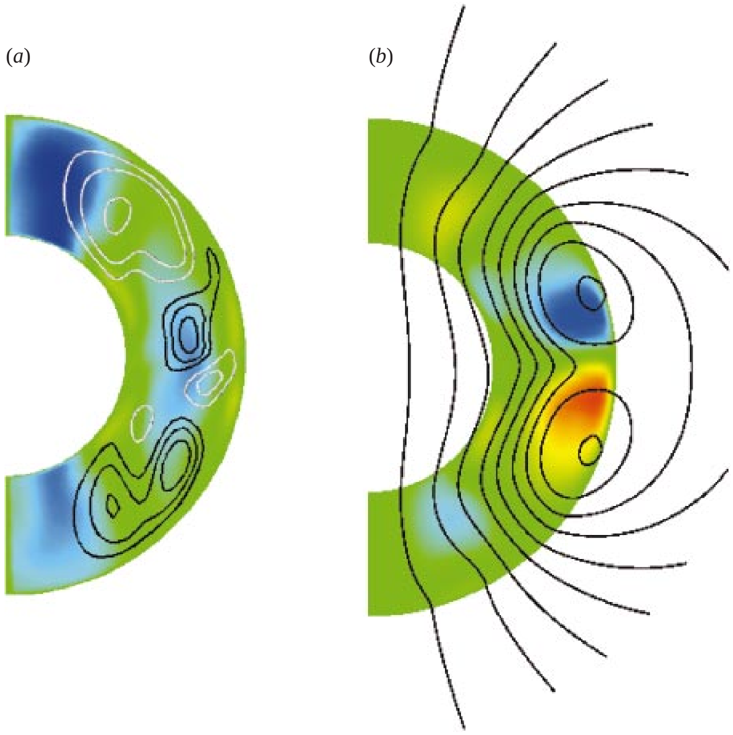

Figure 20. Longitudinally averaged structure of velocity and magnetic fields in a meridional plane. (*a*) Velocity field. The meridional component of velocity is represented by streamlines, with white for clockwise rotation and black for counter-clockwise rotation. Colour map denotes the angular velocity relative to the mean value over the whole spherical shell with red for positive (eastward) and blue for negative (westward). (*b*) Magnetic field. Black lines show the meridional (poloidal) component of magnetic lines which points to the south (downward). The longitudinal (toroidal) component is represented by a colour map with red for positive and blue for negative. There is no longitudinal component in the vacuum outside the spherical shell. $t = 64.1$.

meridional components are shown on a meridional plane with colour map and lines, respectively. We see the well-known characteristics of the axisymmetric components of the velocity and magnetic fields: (i) There is a differential rotation in which the flow near the rotation axis moves faster eastward on the equatorial plane. (ii) The toroidal magnetic field has a pair of strong peaks of opposite sense at low latitude near the outer boundary, and another pair of weaker peaks near the rotation axis. (iii) The poloidal magnetic field has a dipole structure (see Sakuraba & Kono 1999; Christensen *et al.* 1999). It is a common practice that the conversion (ω effects) from the poloidal to toroidal components of magnetic lines is explained by a differential rotation in the longitudinally averaged velocity. We should note, however, that it is difficult to imagine an instantaneous local structure of the velocity and magnetic fields from the longitudinal averages.

There remain several interesting questions on the generation mechanism and structure of the magnetic field. First, why is the magnetic field intensified much more in the second-equilibrium period than in the first? We note that there are two important differences in the structure of anticyclones between the first- and second-equilibrium periods: in the latter, the number of anticyclones is decreased by half, the two-dimensional structure is broken down, and the vorticity is localized near the equatorial plane. These changes may work to strengthen the intensity of the anticyclones themselves and also the magnetic field. Secondly, how is a reversal of the dipole polarity possible? Although no reversal is observed in the present numerical simulation, there is a possible trigger of the reversal. It is the unpredictable direction of weak magnetic flux density near the equatorial plane just after an anticyclone has broken down and the magnetic field associated with it diminishes in the recurrent cycle of creation and annihilation of convection vortices and magnetic field. Thirdly, how general are the mechanisms of magnetic field intensification observed in the present numerical simulation? Varying appearances of the convection field structure depending on the control parameters make us inclined to suppose that there may be many different mechanisms. A comparison of many studies by different authors suggests that the concentration and stretching of magnetic lines, especially in anticyclones, seems to be a common dynamo mechanism (Kageyama & Sato 1997; Olson *et al.* 1999; Katayama *et al.* 1999; Sakuraba & Kono 1999). Recall, however, that there are two completely different types of flow structure of thermal convection depending on the magnitude of the Rayleigh number. The convection inside the imaginary tangent cylinder (a circular cylinder parallel to the rotation axis and tangent to the inner sphere) is more active than that outside if the Rayleigh number exceeds some critical value (Glatzmaier & Roberts 1997; Olson *et al.* 1999). Accordingly, the magnetic field is intensified more inside the tangent cylinder than outside, which is completely different from the situation realized by the present numerical simulation. An interesting challenging problem is whether there is any unified dynamo mechanism applying both inside and outside the tangential cylinder.

The authors would like to express their hearty gratitude to Professor U. Christensen for his critical reading of the original manuscript with many invaluable comments. This work has been supported by a Grant-in-Aid for Scientific Research on Priority Areas (B) from the Ministry of Education, Culture, Sports, Science and Technology of Japan.

REFERENCES

Busse, F. H. 2000 Homogeneous dynamos in planetary cores and in the laboratory. *Annu. Rev. Fluid Mech.* **32**, 383–408.

Christensen, U., Aubert, J., Cardin, P., Dormy, E., Gibbons, S., Glatzmaier, G. A., Grote, E., Honkura, Y., Jones, C., Kono, M., Matsushima, M., Sakuraba, A., Takahashi, F., Tilgner, A. Wicht, J. & Zhang, K. 2001 A numerical dynamo benchmark. *Phys. Earth Planet. Inter.* **128**, 25–34.

Christensen, U., Olson, P. & Glatzmaier, G. A. 1999 Numerical modelling of the geodynamo: a systematic parameter study. *Geophys. J. Intl* **138**, 393–409.

Glatzmaier, G. A. & Roberts, P. H. 1997 Simulating the geodynamo. *Contemp. Phys.* **38**, 269–288.

Grote, E. & Busse, F. H. 2001 Dynamics of convection and dynamos in rotating spherical fluid shells. *Fluid Dyn. Res.* **28**, 349–368.

Ishihara, N. & Kida, S. 2000 Axial and equatorial magnetic dipoles generated in a rotating spherical shell. *J. Phys. Soc. Japan* **69**, 1582–1585.

Kageyama, A. & Sato, T. 1997 Generation mechanism of a dipole field by a magnetohydrodynamic dynamo. *Phys. Rev.* E **55**, 4617–4626.

Katayama, J. S., Matsushima, M. & Honkura, Y. 1999 Some characteristics of magnetic field behavior in a model of MHD dynamo thermally driven in a rotating spherical shell. *Phys. Earth Planet Inter.* **111**, 141–159.

Kida, S. Araki, K. & Kitauchi, H. 1997 Periodic reversals of magnetic field generated by thermal convection in a rotating spherical shell. *J. Phys. Soc. Japan* **66**, 2194–2201.

Kida, S. & Kitauchi, H. 1998*a* Chaotic reversals of dipole moment of thermally driven magnetic field in a rotating spherical shell. *J. Phys. Soc. Japan* **67**, 2950–2951.

Kida, S. & Kitauchi, H. 1998*b* Thermally driven MHD dynamo in a rotating spherical shell. *Prog. Theor. Phys. Suppl.* **130**, 121–136.

Kitauchi, H., Araki, K. & Kida, S. 1997 Flow structure of thermal convection in a rotating spherical shell. *Nonlinearity* **10**, 885–904.

Kitauchi, H. & Kida, S. 1998 Intensification of magnetic field by concentrate-and-stretch of magnetic flux lines. *Phys. Fluids* **10**, 457–468.

Larmor, J. 1919 How could a rotating body such as the sun become a magnet? *Rep. Brit. Assoc. Adv. Sci.* 159–160.

Merril, R. T., McElhinny, M. W. & McFadden, P. L. 1996 *The Magnetic Field of the Earth, Paleomagnetism, the Core, and the Deep Mantle.* Academic.

Olson, P., Christensen, J. & Glatzmaier, G. A. 1999 Numerical modeling of the geodynamo: mechanisms of field generation and equilibration. *J. Geophys. Res.* **104**, 10 383–10 404.

Roberts, P. H. & Glatzmaier, G. A. 2000 Geodynamo theory and simulations. *Rev. Mod. Phys.* **74**, 1081–1123.

Sakuraba, A. & Kono, M. 1999 Effect of the inner core on the numerical solution of the magnetohydrodynamic dynamo. *Phys. Earth Planet Inter.* **111**, 105–121.

Zhang, K.-K. & Schubert, G. 2000 Magnetohydrodynamics in rapidly rotating spherical systems. *Annu. Rev. Fluid Mech.* **32**, 409–443.